

ABSTRACT

NEEYAKORN, WORAKARN. Interfacial Slippage and Friction Studies on Material of Interest to Microelectromechanical Systems. (Under the direction of Jacqueline Krim.)

I have studied the water vapor adsorption onto quartz crystal microbalance crystals in different type of gas surrounding. The noble gas alone has no charge and therefore can not have a Coulomb interaction with the water molecules, only van der Waals interactions. However, the study reveals how dissolved gas increases the hydrophobicity of water, which has the impact on the slip time and sliding friction of water film. This effect strongly influences the slippage of water film. I also performed a quartz crystal microbalance (QCM) study of the nanotribological properties of organo-phosphate (tricresylphosphate and t-butyl phenylphosphate) layers adsorbed from the vapor phase onto silicon (amorphous silicon and MEMS-like polysilicon), and octadecyltrichlorosilane (OTS) treated silicon and gold surfaces. The latter systems have been studied in order to explore whether organophosphates and OTS in combination might prove synergistic from a tribological point of view. There is a strong possibility that this combination will also exhibit synergistic tribological behaviors when tested on actual MEMS devices. Therefore, it is important to perform QCM measurement on silicon that is as close to that of MEMS devices. In order to perform this study, we have developed a deposition method involving a Si-Ge layer that enables the growth of polycrystalline silicon on top of Cu QCM electrodes. The structural and morphological properties of these samples have been characterized with Raman spectroscopy and atomic force microscopy (AFM), confirming that they are similar in nature to the silicon in actual MEMS devices.

**INTERFACIAL SLIPPAGE AND FRICTION STUDIES ON MATERIAL OF
INTEREST TO MICROELECTROMECHANICAL SYSTEMS**

by
WORAKARN NEEYAKORN

A dissertation submitted to the Graduate Faculty of
North Carolina State University
in partial fulfillment of the
requirements for the Degree of
Doctor of Philosophy

PHYSICS

Raleigh

2006

APPROVED BY:

Prof. Jacqueline Krim
Chair of Advisory Committee

Prof. Dave Aspnes

Prof. Hans Hallen

Prof. Arkady Kheyfets

In dedication to my loving grandmother

Tongmark Sangwornrachasup

BIOGRAPHY

I was born in Bangkok, Thailand and graduated from Kaennakorn Wittayalai High School in Khonkaen in 1994. Motivated by science, I participated in DPST program (The Development and Promotion of Science and Technology Talents Project). This allowed me to gain more scientific experiences and improve my intellectual creativity. I attended the Khonkaen University for a year before coming to the United States to pursue my dream of studying physics under Royal Thai Government Scholarship and doing state-of-art physics research. In 1999, I received a Bachelors Degree in Physics with a minor in Applied Mathematics and continued on to pursue a Ph.D. in Physics at North Carolina State University in Raleigh.

I was very much motivated in learning and being able to contribute my creativity thought to the science community. This dissertation has been a major part of my life and it represents the culmination of several years of my study. Being a part of research group at North Carolina State University has given me wonderful experiences which can be very useful to my life and my future career.

ACKNOWLEDGEMENTS

I would like to thank my advisory committee Dave Aspnes, Hans Hallen, Arkady Kheyfets and Jacqueline Krim. Their help in guiding me into the right direction had been invaluable. I specially thank Jacqueline Krim for providing me with the motivation to fuel my scientific creativity to complete my work.

I thank my friends at Nanoscale Tribology laboratory for sharing insightful discussion. I thank Mohamed Abdoumasoud, Tonya Coffey and Manju Varma for their valuable contributions to chapter 3 and 7. I thank my friends at Thai Student Association at NCSU for their support. I thank Malliga Suewattana, who is a lifelong friend and a fellow physicist, for her constant support. I thank Jenny Allen for her help in every kind of legal paper work I needed to deal with.

I thank my family, especially my big brother, Worawee Neeyakorn, who always believes in me and is there when needed. I thank my lovely friend, Tongjit Supapolsiri, for her tireless support.

Finally, I thank my grandmother Tongmark Sangwornrachasub who was bringing me up to be one caring and independent person and always believed that I would become a doctor in science like the King Rama V known as the king who modernized Thailand.

This work has been funded by MURI Extreme Friction Grant

TABLE OF CONTENTS

LIST OF TABLES.....	viii
LIST OF FIGURES.....	ix
CHAPTER I: THE EFFECT OF ENVIRONMENTAL GAS.....	1
1.1 Physics of no-slip boundary.....	1
1.2 Dissolved gas modulates slip	5
1.3 Adsorption	9
CHAPTER II: MEMS LUBRICANT APPLICATION.....	14
2.1 MEMS and its need for Lubrication.....	14
2.2 Self assembled monolayer	15
2.3 Why vapor phase lubrication (VPL)?	16
2.4 Tricresylphosphate as a vapor phase lubricant.....	18
CHAPTER III: EXPERIMENTAL TOOLS.....	20
3.1 Quartz Crystal Microbalance (QCM).....	20
3.2 QCM study of vapor phase lubricant uptakes.....	21
3.3 Relationship between mass uptake and frequency shift	23
3.4 Quality factor	24
3.5 SAMS as release-related solution.....	25
3.6 Octadecyltrichlorosilane (OTS).....	27
3.7 Oscillator circuit.....	29
3.8 Sliding Friction Measurements.....	31
3.8.1 Acoustic impedance of a viscous film.....	32
3.8.2 Acoustic Impedance of a 3-D Gas.....	33

3.8.3 Acoustic Impedance of a Film-Vapor System.....	35
3.9 Damping due to interfacial slippage.....	36
3.10 Experimental determination of quality factor Q	37
3.11 Auger Electron Spectroscopy (AES).....	40
CHAPTER IV: EXPERIMENTAL APPARATUS AND PROCEDURE.....	42
4.1 Experimental Hardware.....	42
4.2 Experimental Procedure.....	45
4.2.1 Sample Preparation.....	45
4.2.2 Calibration.....	46
CHAPTER V: EFFECT OF EXTERNAL GAS TO WATER FILM LAYER.....	48
5.1 Experimental Procedure.....	48
5.2 Result and Discussion.....	51
5.2.1 Water vapor uptake.....	51
5.2.2 Water vapor uptake in N ₂ gas (or Ar).....	52
5.3 Discussion.....	54
CHAPTER VI: VAPOR PHASE LUBRICANT UPTAKE EXPERIMENTS.....	61
6.1 Uptake of lubricants on Ag surfaces.....	61
6.2 Vapor phase lubricant uptakes on ozone-cleaned silicon oxide surfaces.....	65
6.2.1 TCP and TBPP uptakes on amorphous silicon surface	66
6.2.2 TCP and TBPP uptakes on polysilicon surface.....	67
6.2.3 TCP and TBPP uptakes on OTS-coated silicon surface.....	69
6.3 Auger Analysis.....	70
6.4 Discussion.....	73

CHAPTER VII: MEMS APPLICATION	77
7.1 MEMS structure.....	77
7.2 Friction coefficient.....	78
7.3 The comb drive theory.....	84
7.4 Experimental Setup	85
CHAPTER VIII: CONCLUSION AND FUTURE WORK	88
8.1 Impact of environmental gas to the water film layer.....	88
8.2 Future work.....	89
8.3 Vapor phase lubricant uptakes.....	91
8.4 Outlook for MEMS application	93
APPENDIX	100
APPENDIX A.....	101
APPENDIX B.....	106

LIST OF TABLES

TABLE 3.1 Property data of an OTS monolayer coating and oxide layer.....	28
TABLE 5.1 The solubility of nitrogen and argon in water	55
TABLE 5.2 The sticking-rate coefficients normalized to the vacuum system.....	56
TABLE 5.3 Results for neutron reflectivity performed on OTS against different water subphases.....	58
TABLE 6.1 Summary of experimental results of vapor phase lubricant uptakes	73
TABLE 8.1 The solubility of gases in water	90
TABLE 8.2 Summary of experimental results of vapor phase lubricant uptakes	92

LIST OF FIGURES

FIGURE 1.1 Shows the flow past three different surfaces.....	2
FIGURE 1.2 A schematic diagram of microchannel experiment setup.....	4
FIGURE 1.3 Velocity profiles for flow over a hydrophobic and hydrophilic surface.....	5
FIGURE 1.4 Show the onset of slippage of fluid	7
FIGURE 2.1 Show TCP reaction films	19
FIGURE 3.1 The quartz crystal microbalance crystal	21
FIGURE 3.2 The quartz crystal axes and cut angle.....	22
FIGURE 3.3 The structure of SAMs	26
FIGURE 3.4 Deposition of a self-assembled polysiloxane	27
FIGURE 3.5 Structure of SAMs (octylphosphonate and octadecylphosphonate).....	28
FIGURE 3.6 Pierce oscillator circuit	30
FIGURE 3.7 The diagram of mixer circuit	31
FIGURE 3.8 The Auger process	41
FIGURE 4.1 Vacuum system of the QCM experiment	43
FIGURE 4.2 A diagram of experimental setup	44
FIGURE 4.3 QCM crystal and ceramic crucible.....	44
FIGURE 5.1 A diagram of experimental setup (side view)	49
FIGURE 5.2 A diagram of experimental setup (top view)	50
FIGURE 5.3 Frequency shift and inverse quality shift for water vapor uptake on gold surface in vacuum.....	51

FIGURE 5.4 Inverse quality shift and deposited mass for water vapor uptake onto gold surface in vacuum, nitrogen and argon environment.....	53
FIGURE 5.5 Illustrate the possible shape of water droplet.....	60
FIGURE 6.1 A diagram of vacuum setup and Crystek quartz crystals	60
FIGURE 6.2 Frequency shifts of QCM crystals during lubricant uptakes	62
FIGURE 6.3 Inverse quality shift and deposited mass for vapor phase lubricant uptake on amorphous silicon surface.....	66
FIGURE 6.4 Inverse quality shift and deposited mass for vapor phase lubricant uptake on polycrystalline silicon surfaces.....	68
FIGURE 6.5 Inverse quality shift and deposited mass for vapor phase lubricant uptake on OTS-coated amorphous silicon surfaces.....	69
FIGURE 6.6 Auger surface scans of VPL/OTS-coated silicon surface	71
FIGURE 6.7 AFM images of silicon samples	72
FIGURE 6.8 Illustrate the structure of SAMs and how TCP is trapped into the void....	74
FIGURE 7.1 Sidewall friction tester	77
FIGURE 7.2 Wire-bonding diagram	79
FIGURE 7.3 A diagram of the area where contact is made	80
FIGURE 7.4 Closer view of the area where contact is made	80
FIGURE 7.5 The schematic digram of the MEMS comb drive	85
FIGURE 7.6 The vacuum system housing the MEMS devices	86
FIGURE 7.7 The vacuum system housing the MEMS devices	87
FIGURE A1 The diagram of silicon growth with MBE.....	102

FIGURE A2 AFM images of polycrystalline silicon surfaces with growth temperature of 400 °C.	103
FIGURE A3 AFM images of polycrystalline silicon surfaces with growth temperature of 375 °C and 350°C	104
FIGURE A4 Raman Spectroscopy of silicon sample surfaces.....	105
FIGURE B1 The front panel diagram of Labview program for QCM uptake measurement.....	106
FIGURE B2 The block diagram of Labview program for QCM uptake measurement	107

CHAPTER 1

IMPACT OF ENVIRONMENTAL GAS

1.1 Physics of no-slip boundary

For several hundred years one usually relies on the assumption that, when fluid flows over a solid surface, the liquid molecules adjacent to the solid are stationary relative to the solid and the viscosity is equal to the bulk viscosity [1]. Scientists and engineers have applied the no-slip boundary condition at the solid surface. Navier first proposed a general boundary condition that incorporates the possibility of fluid slip at a solid boundary. Navier's proposed boundary condition states that the velocity at a surface is proportional to the shear stress at the surface:

$$v_s = \beta(dv_x / dy) \quad (1.1)$$

Here, v_s is the slip velocity and the term in parenthesis is the local shear rate. β is a constant called slip length. The slip length is the distance behind the interface at which the fluid velocity extrapolates to zero. The no-slip boundary condition is hold when β is zero.

The physics of no-slip boundary states that flowing fluid comes to rest just at the point where it meets the solid surface [2]. At the macroscopic level, it is well accepted that the boundary condition for a viscous fluid at the solid wall is one of "no-slip." The fluid velocity matches the velocity of the solid boundary. Since the no-slip condition holds true for several rough surface systems, it is intuitively obvious to think that surface roughness promote stick. The viscous dissipation as fluid flows past surfaces irregularities brings it to rest. Some molecular dynamics simulations confirm slip past surfaces that lack any lateral corrugation of the potential of interaction with the fluid [3-4]. This situation is hypothetical

because, in a real world, the surface pins the flowing liquid. Realistic walls do possess structure and those points of localized preferential attachment produce stick. The effects of topographical irregularity on fluid flow cause the pinning flowing liquid to the surface. This is illustrated in figure below. In figure 1a, nothing pins the fluid to the wall. In figure 1b, the fluid is pinned to the wall by corrugation of the wall potential, except if the fluid–fluid cohesive forces exceed the fluid–wall attraction. In figure 1c, the fluid is pinned to the wall by flow irregularities even if the fluid wets the wall only partially. It was also suggested that the irregularity can also be chemical [5].

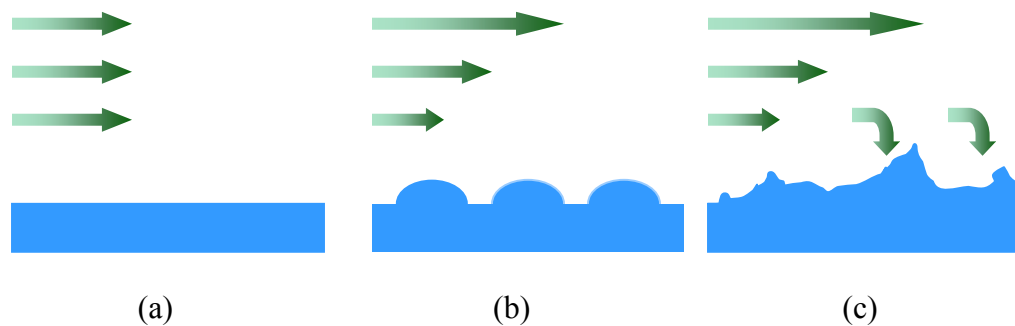
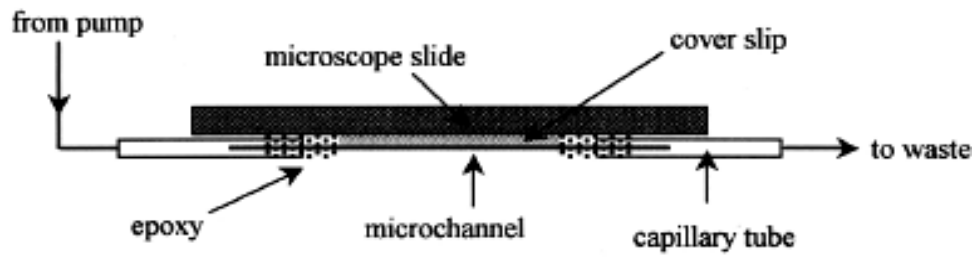


Figure 1.1 Show the flow past three different surfaces: a) an absolutely smooth wall b) a wall with corrugation at the atomic level in the surface potential and c) a surface whose roughness, larger than the molecular fluid. The length of the arrows indicates velocity of the moving fluid.

Several experimental results confirm that the no-slip condition is accurate for a number of macroscopic flows. However, will this always be true for all systems? Recent experiments and simulations show that the textbook assumption of no slip at the boundary can fail greatly when walls are sufficiently smooth. Typical magnitudes of the slip length reported in the literature are submicrometer, so small that the practical consequence of slip would be minimal for flow in channels whose size is macroscopic. But if the channel size is very small, the potential ramifications in microchannels and nanochannels are major.

Furthermore, the recent progress in nanotribology clearly shows that the laws of macroscopic friction are inapplicable at the atomic scale. For example, Pit et al. reported slippage of hexadecane on wetted sapphires surfaces [6]. Craig et al. inferred slip from force measurements on partially hydrophilic surfaces with contact angle of 70° in aqueous sucrose solution [7]. Zhu and Granick also observed that the onset of slip varied systematically with contact angle [8]. Furthermore, Trethewey and Meinhard of University of California at Santa Barbara used Micron-resolution particle image velocimetry to measure the velocity profiles of water flowing through $30 \times 300 \mu\text{m}$ channels. They reported that the apparent slip velocity, which is measured just above the solid surface, is not equal to zero for water flowing through a microchannel coated with hydrophobic octadecyltrichlorosilane. This slip velocity is approximately 10% of the free-stream velocity and yields a slip length of approximately $1 \mu\text{m}$ as shown in Fig 1.2 (taken from ref. [9]). However, the measured velocity profiles are consistent with the solution of Stokes' equation (see Figure 1.3) when the surface is hydrophilic [9].



(a)

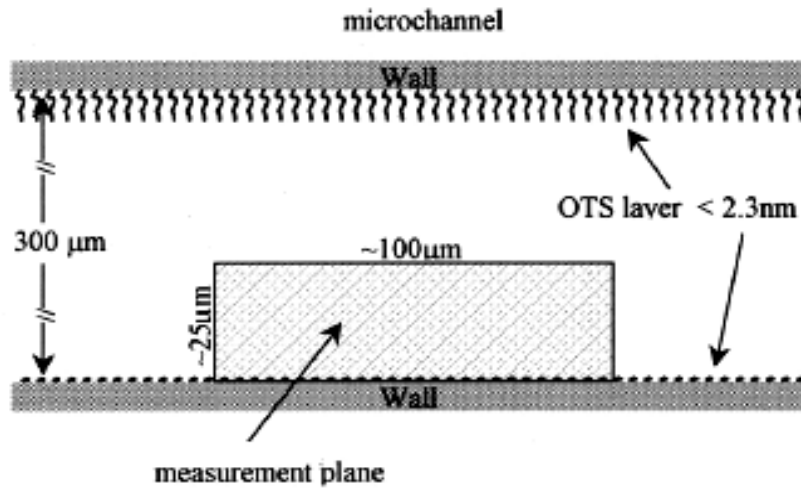


Figure 1.2 A schematic diagram of microchannel experiment setup by Tretheway and Meinhart [9].

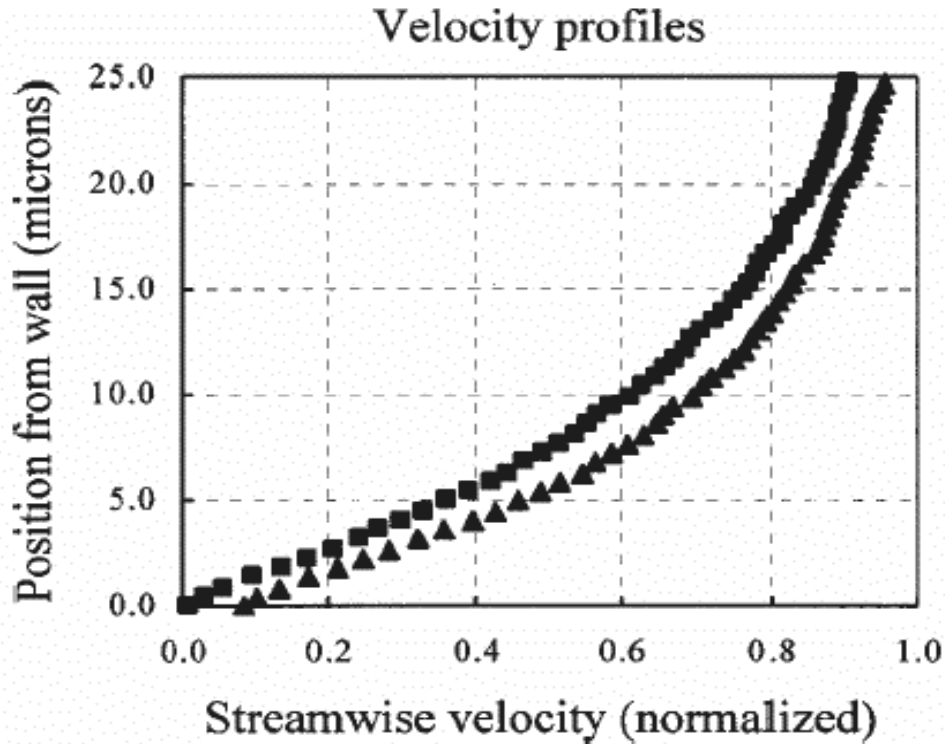


Figure 1.3 Velocity profiles for flow over a hydrophobic (triangle) and hydrophilic (square) microchannel surface. The velocity profiles are normalized by the free-stream velocity [9].

With the assumption that the slip velocity is proportional to the shear stress, Ruckenstein and Rajora [10] suggest that entrained or soluble gases in the flowing liquid may increase fluid slip by forming a gap between the liquid and the wall, thereby increasing the slip length β . The current working fluid is deionized water.

1.2 Dissolved gas modulates slip

Recent experiments show partial slip of so-called Newtonian fluids, such as alkanes and water. Granick et al. discover the systematic deviations from the predictions based on the no-slip boundary condition. They performed experiments in which the surface force apparatus was used to measure hydrodynamic forces of Newtonian fluids that had been purged with various gases. The surface-surface spacing of 10–100 nm substantially

exceeded the size of the fluid molecules, therefore the fluid responded as a continuum. The spacing was vibrated with vibration frequency of 9 Hz and with small amplitude. The hydrodynamic force was measured as a function of the ratio v_{peak}/D suggested by Reynolds equation [11].

$$F_H = f^* \frac{6\pi R^2 \eta}{D} \frac{dD}{dt} \quad (1.2)$$

The deviation of the dimensionless number f^* from unity quantifies the deviation from the classical no-slip prediction. The classical prediction is analogous when the surface spacing is vibrated. In that case a sinusoidal oscillatory drive generates an oscillatory hydrodynamic force whose peak we denote as $F_{H,peak}$. The peak velocity of vibration is $v_{peak} = d\omega$ where d is vibration amplitude and ω the radian frequency of vibration. Studies show that when the frequency and amplitude of oscillatory flow are varied, results depend on their product, v_{peak} , and that deviations from equation (1) depend on v_{peak}/D .

The figure 1.4 shows results of simple newtonian fluids flow past atomically smooth surfaces, either wetted or partially wetted. The hydrodynamic force $F_{H,peak}$ is plotted against reduced flow rate, v_{peak}/D such that a straight line of slope unity would indicate ‘no-slip’ assumed by equation (1). The fluid was saturated with carbon dioxide (filled symbols) or argon (open symbols). Their experimental results showed the no-slip condition was obeyed when the tetradecane had been saturated with carbon dioxide gas. However, massive deviations from this prediction were found when the tetradecane was saturated with argon. This makes it seem likely that argon segregated to the solid walls, creating a low-viscosity boundary layer, in this way greasing the flow of fluid past that surface. Presumably, the amount of segregation is a materials property of the fluid, the chemical makeup of the surface, and the chemical identity of the dissolved gas. In this example, the fact that argon

possesses low solubility in tetradecane may have made it more prone to segregate to the surfaces [5]. Therefore, low solubility of environmental gas plays an important role to the slippage at substrate surface.

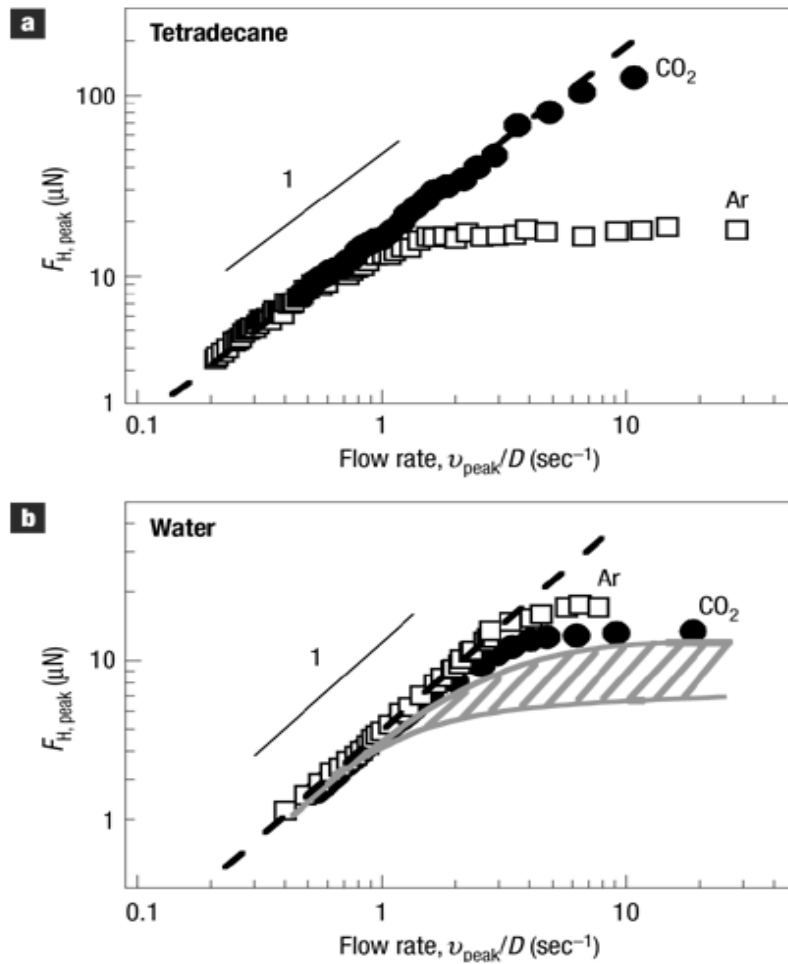


Figure 1.4 Show the onset of ‘slip’ depends on dissolved gas: a) Tetradecane flowing between the asymmetric case of a wetted mica surface on one side, a partially wetted surface of methyl-terminated self-assembled monolayer on the other side b) Deionized water flowing between mica surfaces that are wetted by this fluid. The hatched region of the graph shows the range of irreproducible results obtained using deionized water such that gases dissolved in the water were not controlled [5].

It was suggested that the reasons for this seem to involve materials chemistry interactions that can be controlled – especially wettability and the presence of trace

impurities, even of dissolved gases [5]. Vinogradova was the first to attempt to explain a possible mechanism of the genesis of this layer [11]. Later on De Gennes then conjectured that shear may induce nucleation of vapor bubbles; once the nucleation barrier is exceeded the bubbles grow to cover the surface, and flow of liquid is over this thin gas film rather than the solid surface itself. Indeed, it is likely that incomplete air removal from the solid surfaces can profoundly influence findings in these situations where surface roughness is so low. It is identified by recent research as a likely source of the miss-named long-range hydrophobic attraction [12, 13]. Gases also appear to influence the sedimentation rate of small particles in liquid [14].

One of the main goals of this study is to study the impact of environmental gases exterior to the lubricant-substrate interface on nanodynamical properties in controlled vacuum chamber. This can be done using QCM technique. Results can be compared qualitatively to those results from surface force apparatus experiments which were not carried out in controlled vacuum chambers. In the following, we will employ a QCM to study various aspects of this problem:

- (1) Impact on friction of an external gas: The results of this study will be profit to micromechanical devices developed for space application use. This is because MEMS, which are susceptible to friction and wear, would have to operate in the vacuum or maybe in different type of environmental gases.
- (2) Sliding friction of material of interest to MEMS: To be able to prevent the failure of MEMS devices when in use, we must overcome the problems and have better understanding of the fundamental physics of mobile MEMS lubricant and physics of interfacial sliding.

1.3 Adsorption

Adsorption is the process in which atoms or molecules of a substance in one phase (usually gas) become bonded to the surface of a second substance in a different phase (usually solid). Adsorption is to be distinguished from absorption, the process in which one substance interpenetrates the bulk volume of a second substance. There are many examples of adsorption in everyday life. Activated charcoal, which can have a surface area of up to several thousand square meters per gram, is capable of adsorbing many different substances. It is used to filter contaminants from drinking water, and is also used in gas masks to remove toxic substances from breathing air. Silica gel (SiO_2) packets, which adsorb water vapor, are often packed in with moisture sensitive merchandise. And adsorption is a key part of many catalytic processes, as many chemical reactions will not take place except in the presence of a particular kind of surface. For example, molecular hydrogen and oxygen can be mixed at room temperature with no effect. However, these molecules dissociate when adsorbed on a platinum surface, and will then combine to form water molecules. We will be discussing a system where a substance in the gas phase becomes bonded to the surface of a second, solid substance.

Adsorbate is the substance originally in the gas phase which becomes bonded to the surface of a second, solid substance: adsorber or adsorbent. Generally, there are two types of adsorption processes, characterized by the strength of the bond between the adsorbate and substrate: the physisorption or chemisorption.

1. Physical adsorption or physisorption: the bonds between atoms or molecules being adsorbed and the substrate are due to dipole-dipole interactions, and are relatively weaker

than chemical adsorption. Physisorption is often characterized by much shorter residence time than chemisorption.

2. Chemical adsorption or chemisorption: a chemical bond is formed between the adsorbate and the substrate. Such bonds, which involve the exchange or sharing of electrons between the adsorbate and the substrate, are much stronger. Typical physisorption binding energies are 50-500 meV per atom or molecule; chemisorption binding energies are typically an order of magnitude greater.

Some significant differences between physisorption and chemisorption:

1. Physisorption is reversible, i.e., the adsorbate will desorb (become unbound from the substrate) when the substrate temperature is raised, and return to its original condition in the gas phase. Chemisorption is usually not reversible; i.e., raising the substrate temperature will typically not result in the adsorbate returning to its original condition in the gas phase.

2. Physisorption does not result in the dissociation of adsorbed molecules. Chemisorption often results in the dissociation of molecules during the adsorption/chemical reaction process.

3. With physisorption, multiple layers of the adsorbate can form on the substrate. Chemisorption is typically characterized by the formation of a single layer of adsorbate on the substrate.

4. Chemisorption typically occurs over a wide range of temperatures, often exceeding temperatures at which the adsorbate will condense from the gas phase to the liquid phase. Physisorption occurs with the substrate temperature typically near or below temperatures at which the adsorbate will condense from the gas phase to the liquid phase.

In physisorption, the force of attraction between adsorbate and substrate is due to instantaneous fluctuating electric dipole moments in both the atoms or molecules of the adsorbate and the atoms of the substrate. Even in an atom or molecule with no permanent electric dipole moment, fluctuations in the electron charge distribution will give it an instantaneous (short lived, but averaging to zero over a longer time interval) dipole moment which will induce a dipole moment in a nearby atom or molecule. The interaction between the original and induced dipole moments results in an attractive force between these two moments. Such dipole-dipole forces are known as van der Waals forces.

In addition to being the main force resulting in physisorption, the van der Waals force is the main force resulting in the condensation and solidification of inert atoms (e.g., Ne, Ar, Kr) and many simple molecules such as N₂, O₂ and CH₄. In this experiment, we will explore the adsorption of inert atoms like Argon and simple nitrogen molecules on gold substrate surfaces.

In 1990s, Langmuir proposed that adsorbates were bound to the adsorbent surface at specific sites only and these adsorptions were marked by uniform binding energy. Subsequent gas particles attempting to impinge or adsorb on occupied sites will rebound into the gas phase. Thus, only one monolayer is formed and any surface interaction or diffusion of adsorbates is excluded. As a result, the Langmuir Adsorption Isotherm is given as shown in equation below.

$$\theta = \frac{C_1 \chi(T) P}{1 + C_1 \chi(T) P}, \quad \text{with } \chi(T) = \frac{\exp\left(\frac{\Delta H_{ads}}{kT}\right)}{C_1} \quad (1.3)$$

In the equation, C_1 is a constant which is equal to $kT/q\lambda^3$ and θ is the fraction of a surface covered by an adsorbed layer in thermal equilibrium as a function of vapor pressure P . ΔH_{ads} is the adsorption or binding energy.

The fraction coverage starts out linearly proportional to ambient pressure at low pressure and asymptotically approaches unity at high pressure. One can also assume that all the particles adsorb independently of one another. This is a nonlocal adsorption whereby adsorbates are free to move around. This implies that the adsorption energy, ΔH_{ads} , and consequently the residence time, τ_a , are independent of the surface population, N_a . This model is known as Henry's law and is relevant to systems with very weakly bound adsorbed particles. The Henry's law for 2-dimension gas adsorption is given by:

$$\frac{N_a}{A} = \chi'(T)P \text{ and } \chi'(T) = \frac{\exp\left(\frac{E_0}{kT}\right)}{C_2} \quad (1.4)$$

Here, C_2 is a constant which is equal to $kT/q\lambda^3$.

However, Langmuir model does explicitly forbid the possibility of adsorption beyond monolayer. Adlayers with many atomic layers thick are not uncommon in physical adsorptions. In 1938, Brunauer, Emmett and Teller had modified the model which allowed the possibility of multilayer adsorption. Their model is called BET model and it becomes a powerful tool for determining surface areas.

It is the fact that that it takes one second to form a monolayer at pressure of 10^{-6} Torr. Here we can take the sticking coefficient in the vacuum system to be equal to one and the sticking coefficients of atom, normalized to the one in vacuum system, on substrate surfaces in room temperature can be calculated from gas adsorption experiments. Sticking coefficient, according to surface chemistry definition, is the ratio of the rate of adsorption to

the rate at which the adsorptive strikes to total surface. It is usually a function of surface coverage, of temperature and of the details of the surface structure of the adsorbent. In this study, the surface area of each experimental run is kept constant. Since temperature is kept constant here, equation 1.3 can be simply rewritten as:

$$\theta = \frac{KP}{1 + KP} \quad (1.5)$$

In the equation K is equal to $K = \chi(T)C_1$ and can be considered as an equilibrium constant. The value of K at various temperatures is normally determined from Langmuir isotherm. However, the temperature is constant in this study. K is therefore a constant. Also the binding energy ΔH_{ads} can be obtained via van't Hoff equation:

$$\left(\frac{\partial \ln K}{\partial T} \right) = \frac{\Delta H_{ads}}{RT^2} \quad (1.6)$$

$$\Delta H_{ads} = RT^2 \left(\frac{\partial \ln K}{\partial T} \right) \quad (1.7)$$

CHAPTER 2

MEMS APPLICATION

2.1 MEMS and its need for lubrication

Microelectromechanical systems (MEMS), the integration of miniaturized mechanical components with microelectronic components, are a billion-dollar industry. However, the commercialization of many MEMS devices-such as rotary gears, microturbines and relay switches is held back by tribological issues. Traditional lubricants such as oil would not solve the problem since their micro structures succumb rapidly to capillary forces presence of liquid. Furthermore, most micromechanical devices are susceptible to friction and wear. As a result, there are no commercially available MEMS devices that involve surfaces in sliding contact. Developing reliable coating processes and suitable lubricants for industrial mass-production purposes present major challenges in the MEMS arena [15].

Most approaches published in the MEMS lubrication utilizing hard coatings such as diamond-like carbon [16,17], carbides, nitrides [18] and oxides[19] or hydrophobic organic coatings such as self-assembled monolayers (SAM) [20, 21]. Although these approaches have greatly made improvement in conformal coating and reduction of friction as well as reduced wear in laboratory tests, they have technical limitations relating to their durability. Solid lubricant coatings and SAMS have been shown to wear off during operation [22, 23].

This study is to explore the use of adsorption of vapor phase lubricant as a new means of MEMS device lubrication. Being delivered in the vapor phase, the lubricant will find its way much more easily to the crevices, which these devices are full of. Also the

replenishment property of the vapor phase lubricants will prove to be extremely useful for the lubrication of these micromachining.

2.2 Self-Assembled Monolayer

One of major concern for MEMS industry is the stiction or unintentional adhesion. In the final rinsing stages of the sacrificial oxide layer etch, the etchant is rinsed and the microstructure is dried through evaporation to obtain the free-standing structure. However, there is a high possibility that parts of microstructures can get stuck to nearby surfaces due to the capillary action induced by the droplet in the gap. This may render the device useless if even after drying, the adhesive forces between the contacted areas are more than the restoring forces.

There have been a lot of efforts putting in this field to find the solution. Revising the surface to reduce contact area, changing the water meniscus shape, supercritical drying, freeze sublimation drying have been one of the many approaches devised to avoid release related stiction. However, these techniques are not applicable during the operation of the device. One of promising approaches is using self-assembled monolayers (SAMs). SAMs are molecular assemblies that are formed spontaneously by the immersion of an appropriate substrate into a solution of an active surfactant in an organic solvent. With SAMs, performance is definitely improved but the coating may wear off during operation. This can lead to device failure. Therefore, lubricating the device is necessary for long term reliability. In the next section, vapor phase lubricant will be discussed.

2.3 Why Vapor Phase Lubricants?

In the macroscopic world, there are four types of high temperature lubricants. The first one is solid-lubricant coatings. As mentioned before, there are major limitations in their durability due to wear and moving surfaces thus need to be recoated as the original coating is being worn away. Second one is self-lubricating composites which are contained as a percentage of the bulk material. As surfaces rub against each other, the lubricant at the surface is worn away. This same wear process uncovers fresh solid-lubricant. The third type is lubricating powders: This kind of lubrication introduces either hard particles or solid lubricating powders between the sliding surfaces [24], [25]. The last type is vapor-phase lubrication. Vapor phase lubrication occurs via three distinct forms: organic films which are intentionally reacted with a surface to form a solid lubricating film, vapors which condense to form a lubricating liquid film on the surface of interest and lightweight hydrocarbon vapors deposited onto hot catalytic nickel surfaces.

Most of solid lubricating films on the surface are formed by the reaction between the gas and the surface material. This may or may not consume the surface material in the formation of the lubricious film. Some examples include decomposition of TCP (Tricresyl-phosphate) when exposed to iron surfaces to form an anti-wear, anti-corrosive lubricating film. Abdelmaksound, Bender and Krim at North Carolina State University, report a quartz crystal microbalance study of the nanodynamical properties of TCP reaction films formed on high purity Fe, Cr, Fe oxide, and Cr oxide surfaces at elevated temperatures [26]. In microscopic scale, the QCM data provide the first documentation of trace levels of interfacial slippage, potentially in conjunction with viscoelastic effects, for reaction films characterized

by very low macroscopic friction coefficients. Furthermore, no interfacial slippage is detected in systems exhibiting high friction coefficients.

In addition, it is a well-known fact that, on the microscopic scale, technology demands and challenges are pushing machines towards even smaller and smaller dimensions. Micro/Nano Electro-Mechanical Systems (MEMS/NEMS) industries are growing and expanding very rapidly. Some of these microscopic machines have already found their way to the market like air bag actuators in automobiles, for example. However, one of their main application concerns is how to overcome problems caused by stiction, friction and wear of its tiny moving parts. As these very minute parts are rubbing against the holding substrate and against each other, there is a fairly high chance that they stick together causing machine failure. The question is how to lubricate these very small machines efficiently to guarantee smooth and reliable operations. In addition, some of these devices are intended for extreme environment applications, i.e., excessive high temperature and/or pressure, which are the very typical conditions for VPL. One way to address these concerns is through the very promising application of VPL techniques to lubricate the MEMS/NEMS devices [23].

Being delivered in the vapor phase, the lubricant will find its way much more easily to the crevices, which these devices are full of. Also the replenishment property of the vapor phase lubricants will prove to be extremely useful for the lubrication of these micromachining. These micromachining devices have had a problem with stiction, friction and wear. SAMs coating has come a long way to relieve the stiction problem but SAMs degrades at high temperature 400 °C. The deterioration of the lubrication layer has effects on the long term reliability of the device. One proposed method for maintaining the lubricating coating for a range of temperatures and environments is to use a two phase coating. The first

phase is a chemically bound layer such as octadecyltrichlorosilane (OTS) $\{C_{18}H_{37}SiCl_3\}$. On top of the SAMS layer, the second coating could be a mobile layer: Organophosphates such as Tricresylphosphate [TCP] $\{C_{20}H_{21}O_4P\}$. Since SAMS coating is vulnerable to the high temperature, the second phase would heal the damaged coating by covering exposed surface with high temperature vapor phase lubricant. This study confirms that the vapor phase lubricant molecules, such as TCP molecules, would get trapped to the side of hydrocarbon chain of SAMS and could help protecting the exposed surface.

2.4 Tricresylphosphate as a vapor phase lubricant

Tricresylphosphate or TCP $((CH_3C_6H_4)_3PO_4)$ is a candidate material for vapor phase lubrication, an emerging technology targeted at extreme environment applications that preclude conventional liquid-phase lubricants. The exact theory of how these vapor phase lubricants, TCP in particular, react with different surfaces is far from complete. Wheeler and Faut suggested that the TCP molecule that is deposited at room temperature on an iron surface will decompose upon heating the substrate at a temperature in the range of 150 and 250 °C [27]. TCP molecules fragment upon uptake on certain metals and oxides, forming thick polymeric reaction films above 200 °C through partial corrosion of the underlying substrate (see Figure 2.1).

As mentioned earlier, Abdelmaksound et al. investigated in detail the interaction of TCP with two metal surfaces, namely, iron and chrome. TCP is known to lubricate iron but not chrome. Their discovery bridges the gap between macro- and nanotribology. They reported that reaction films formed on iron oxide or on iron in the presence of oxygen are highly effective lubricants, but are ineffective lubricants when formed on iron, chromium,

chromium oxide, or aluminum substrates [28]. As a result, TCP is a good candidate for this vapor phase lubricant study.

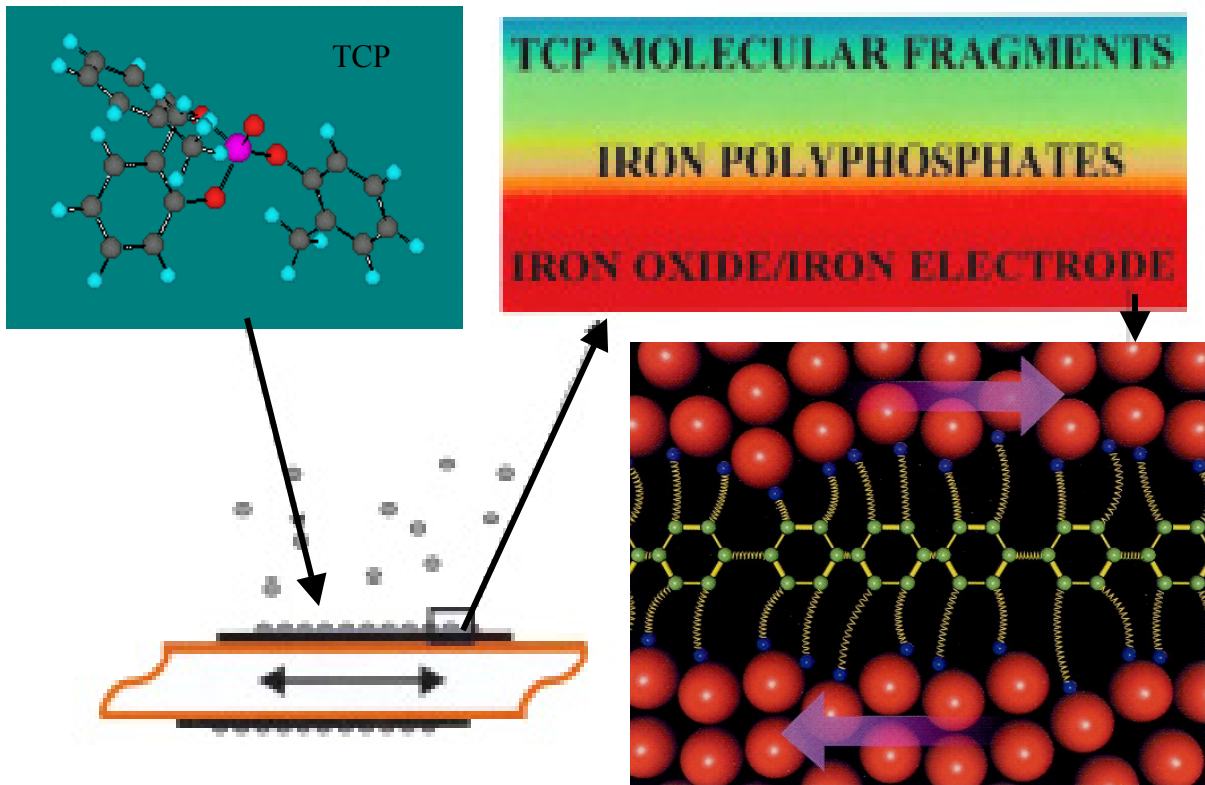


Figure 2.1 TCP reaction films that form on the QCM iron electrodes in the presence of oxygen exhibit trace levels of nanoscale slippage in response to its oscillatory motion [26].

CHAPTER 3

EXPERIMENTAL TOOLS

3.1 Quartz Crystal Microbalance

A quartz crystal microbalance (QCM) consists of a single crystal of quartz that oscillates in transverse shear motion with a high quality factor Q near 10^5 . Metal film electrodes evaporated onto its two major faces serve as the substrates for adsorption studies. The QCM technique is particularly well adapted for measurements of uptake rates of vapor-phase lubricants, providing a sensitive, real-time mean for monitoring mass adsorption from the gas phase, and also tribological properties of the reaction film. QCM is also an attractive technique for comparative studies of macroscopic and microscopic phenomena, owing to the high sliding speeds (up to 2 m/s) and shear rates at which the data are recorded.

Polished grade, 5 MHz, AT-cut (transverse shear mode) QCM crystals were employed for these studies, obtained from Maxtek Inc. with thin layers of silicon and/or Au/Cr metal already deposited onto both sides. The Si films, as prepared by Maxtek, Inc., consist of 1000 Å of 99.999% pure material deposited onto both crystal sides, each of which was prepared with 2900/400 Å thick Au/Cr underlayers.

QCM measurements were also performed on polycrystalline, rather than amorphous, silicon that is similar in nature to the silicon in actual MEMS devices. To achieve MemS-like polysilicon surface, silicon must be deposited onto the Ti layers to a thickness of 1000Å at a temperature of 450°C by solid source Si-Ge molecular beam epitaxy (MBE). This work was done by Sang Min Lee, James Burnett and Robert Nemanich at North Carolina State

University (see Appendix A). Raman Spectroscopy and atomic force microscopy (AFM) are then used to obtain information on the structural and morphological properties of these samples.

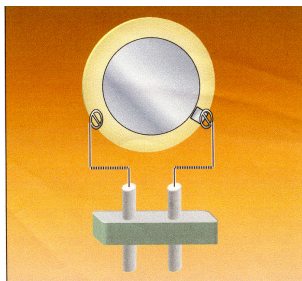


Figure 3.1 Shows the Quartz Crystal Microbalance crystal in its spring clip crystal holder

3.2 QCM Study of Vapor Phase Lubricant Uptakes

For many decades, QCM has been used to monitor the thin film deposition either in vacuum or gas. This technique can measure the frictional force of one-atom-thick films sliding along flat solid surface and was adapted for nanotribological measurements by Krim and Widom in 1986-1988 [29]. Here we will be discussing how to apply this technique to measure the frictional force of monolayer film.

Quartz is a crystalline form of SiO_2 that has solid-solid phase transition at $573\text{ }^\circ\text{C}$. The QCM crystal consists of a thin disk of single quartz crystal, the two faces of which are plated with metal electrodes. When an alternating voltage is applied across the electrodes, the QCM is made to oscillate mechanically at its resonance frequency. It has a relatively high quality factor and high frequency stability.

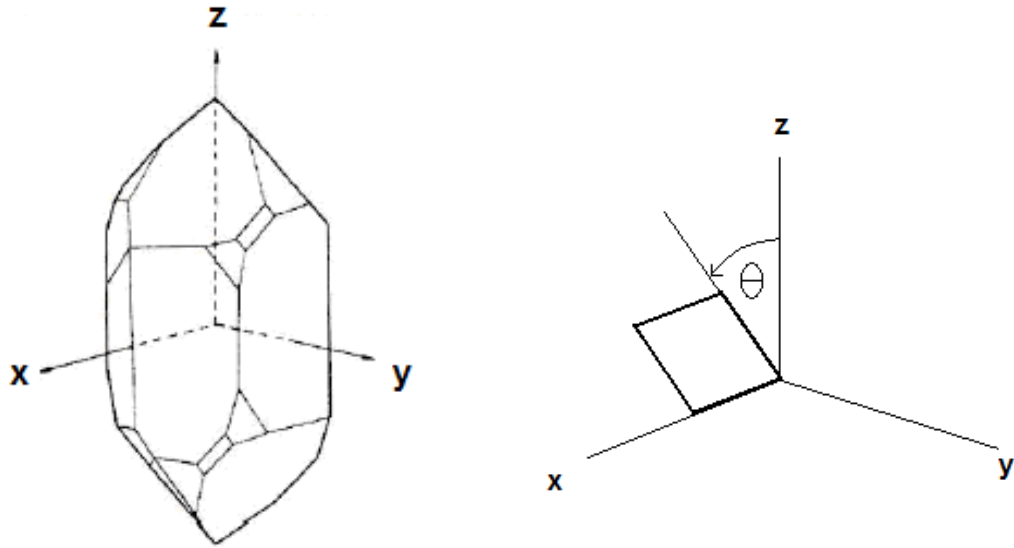


Figure 3.2 a) Quartz crystal axes b) AT-cut crystal with the cut angle, $\theta = 35^{\circ} 15'$

The QCM's used in this work are exclusively AT-cut crystals. This means that crystal oscillates in transverse shear mode, as shown in above figure. Figure 3.2(a) shows the crystallographic axes of the quartz crystal. The Z-axis is chosen to be parallel to the quartz trigonal axis. It is so called because it has three symmetric diagonal axes perpendicular to it. The x-axis is chosen parallel to one of the diagonal axes. The piezoelectric effect depends greatly on direction, for example, if stress is applied along the Z axis, no electric signal is generated. Therefore, the way the quartz disk is cut has a great impact on the crystal frequency as well as its stress and temperature responses. For example, the AT- and BT-cuts are oriented at angles of $\theta = 35^{\circ} 15'$, figure 3.2(b), and $\theta = -49^{\circ}$ respectively from the ZX-plane. AT-cut crystals have zero temperature coefficients near room temperature and high frequency stability and mass sensitivity. Therefore, they are perfect for this study.

3.3 Relationship between mass uptake and frequency shift

In 1957, Sauerbrey investigated the relationship of resonant frequency of quartz crystal to mass deposited on the QCM electrodes [30, 31]. When an alternating voltage is applied across electrodes of an AT-cut quartz crystal, mechanical shear waves are generated across its thickness. Standing waves are established if the thickness of the crystal, t , is an odd integer of $\lambda/2$ where λ is the wavelength of the induced wave. Then, the fundamental frequency f_0 is given by:

$$f_0 = \frac{v_q}{\lambda} = \frac{v_q}{2t} \quad (3.1)$$

where v_q is the speed of wave propagation in quartz. Differentiating and rearranging both sides, one obtains:

$$\frac{df_0}{f_0} = -\frac{dt}{t} \quad (3.2)$$

This can be rewritten in terms of the mass of the quartz, m_q .

$$\frac{df_0}{f_0} = -\frac{dm_q}{m_q} \quad (3.3)$$

In the equation, A is the area of the quartz crystal.

For thin films adsorption onto QCM crystals, if $m_f \ll m_q$, the mass of the added film could be treated as a small perturbation of the quartz oscillator's mass, i.e., dm_q in the last equation could be replaced by m_f . For a film evenly distributed over the active area of the crystal, equations 3.1 and 3.3 can be used to obtain the below relationship.

$$\Delta f = -2 \left(\frac{m_{film} / A}{\rho_q v_q} f_D^2 \right) \quad (3.4)$$

The resonance frequency of quartz crystal depends on the film adsorbed onto the crystal. The adsorbed film causes a drop in the frequency (Δf) which can be rewritten as,

$$\Delta f = - \left(\frac{4 f_{res}^2}{Z_q} \right) \cdot \left(\frac{m}{A} \right) \quad (3.5)$$

Z_q is the transverse acoustic impedance of the quartz ($Z_q = 8.862 \times 10^6$)

m is the mass of the film

A is the area of the electrode.

3.4 Quality Factor

The quality factor “Q” is a dimensionless quantity that has been used in both mechanical and electrical oscillating systems to represent the degree of damping of the oscillator. It is defined as:

$$Q = 2 \pi (\text{Energy stored in one cycle} / \text{Energy lost in one cycle}) \quad (3.6)$$

Energy is stored in the system by the driving mechanism and it is dissipated due to internal friction and external damping forces. From the definition of the Q factor, it is obvious that its inverse is the dissipation factor. Therefore, a high Q means low loss and high frequency stability. The maximum attainable Q of a crystal is a function of the diameter and surface curvature of the blank quartz and is inversely proportional to the frequency of oscillation. When mass is added to the oscillator the overall dissipation is just the sum of the individual dissipations in the mass plus the quartz:

$$\frac{1}{Q} = \frac{1}{Q_q} + \frac{1}{Q_m} \quad (3.7)$$

With added mass, acoustic losses in the material increase and Q decreases further. When the Q factor of the QCM becomes exceedingly low, its oscillation will not be sustained and the crystal will cease to function. Changes in Q can be monitored via changes in the QCM amplitude.

3.5 SAMS as release-related solution

One of the major concern for MEMS industry is the stiction, friction and wear of the microstructure. Stiction is unintentional adhesion. After the last MEMS release procedure, parts of microstructures can get stuck to nearby surfaces when restoring forces are unable to overcome interfacial forces such as capillary, chemical, van der Waals, and electrostatic attractions. There have been a lot of efforts putting in this field to look for the solution and SAMS approach is very promising.

Self-assembled monolayers (SAMs) are molecular assemblies that are formed spontaneously by the immersion of an appropriate substrate into a solution of an active surfactant in an organic solvent [32]. The SAMS-coated surface of MEMS device becomes hydrophobic and greatly reduces the release-related stiction.

Each of these SAMs molecules consists of three main parts as shown in figure 3.3. The first part is the head group, which chemisorbs to the surface. Because of the strong interaction between the head group and the substrate, the molecules attempt to adsorb at all surface sites, resulting in a close-packed monolayer. The second part of the monolayer is alkyl-chain backbone. Van der Waals interactions between chains further contribute to the ordering of the monolayer. The third part is the terminal group. The simplest terminal

functionality is a methyl group; however, the chain may be terminated with a number of different groups such as NH_2 , OH , or COOH , allowing SAMs to be tailored to a particular application. Functionalization of the end group also allows multiple layers to be adsorbed on top of the monolayers [32].

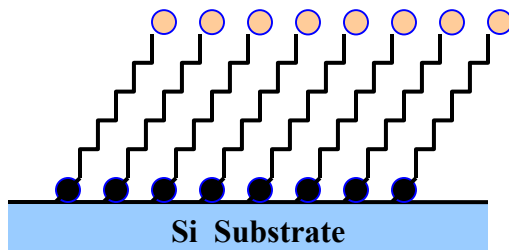


Figure 3.3 The structure of SAMs consists of chemisorbing headgroup (black circles : Si), backbone (hydrocarbod chain) and tail (lightly shaded circles : CH_3)[33].

For the past years, chlorosilane-based monolayer coatings which function as anti-stiction layers for MEMS devices have received much attention. Chlorosilane-based SAMs have the general formula $\text{R}_{4-n}\text{SiCl}_n$, where n , the number of chlorine atoms, can have a value of 1, 2 or 3 only. The tail group(s), R , may be hydroxylated, fluorinated or otherwise functionalized carbon chains or aromatic substituents. In the case of $n < 3$, each R is not necessarily the same.

The figure 3.4 illustrates the reactions that are involved in attaching chlorosilane precursors to silicon surfaces. The first reaction is the hydrolysis on the Si-Cl bonds to form Si-OH bonds and HCl . To complete the hydrolysis reaction, n molecules of water and HCl are needed. After the silanol form of the precursor is generated on the surface, some of the $-\text{OH}$ groups participate in a condensation reaction with a $-\text{OH}$ group on the oxidized silicon surface. This process liberates one water molecule per condensation reaction. The exact fate

of every Si-OH bond in tri- and di-chlorosilanes is uncertain, since cross-polymerization (condensation reactions with other precursor molecules) also occurs.

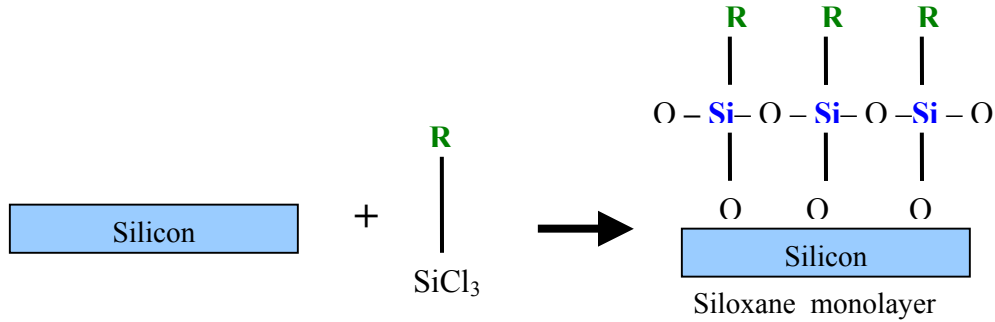


Figure 3.4 Deposition of a self-assembled polysiloxane.

3.6 Octadecyltrichlorosilane (OTS)

OTS is chlorosilane-based monolayer coating which functions as anti-stiction layers for micromachines have received much attention as anti-stiction treatments for silicon MEMS devices. The coefficient of static friction is greatly reduced as shown in table 1. Moreover, the commercial availability of the chlorosilane precursors, and the apparent simplicity of coating process make them attractive to a wide variety of researchers. The availability of a wide variety of functionalized tail groups also make chlorosilanes a useful intermediate to many applications such as the control of the protein binding on silicon-based devices. However, the coating is not particularly wear resistant and decompose in air at 225°C or lower, depending upon the environment [34, 35]. Therefore, having another type of protecting layer for OTS layer might be ideal.

Table 3.1 Property data of an OTS monolayer coating and oxide layer [34].

Film Type	Contact Angle Water	Work of Adhesion $\mu\text{J}/\text{m}^2$	Coefficient of Static Friction
OTS [32]	110	12	0.07
Oxide [32,39]	~ 0-30	~ 20,000	1.1

Chlorosilanes have the general formula $\text{R}_{4-n}\text{SiCl}_n$, where n, the number of chlorine atoms. The tail group(s), R, may be hydroxylated, fluorinated or otherwise functionalized carbon chains or aromatic substituents. OTS has three Si-Cl bonds and one long (18-carbon) alkane chain bound to the chlorosilane group. Chain length is also observed to affect the quality of the monolayers, as indicated by contact angle analysis.

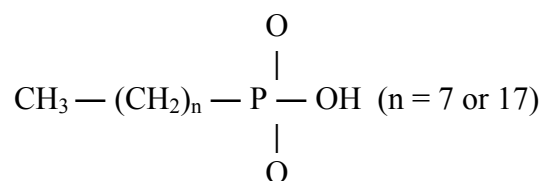


Figure 3.5 Structure of SAMs: octylphosphonate and octadecylphosphonate (ODP)

After SAMS coating, the surface becomes very hydrophobic. According to the study by Tambe and Bhushan, the hydrophobicity depends on the length of hydrocarbon chain of SAMs. Their study measured the contact angles of SAMs coating on the Al and Si substrates. The coatings deposited on Al substrates were alkyl chain phosphonic acid precursors with 8 and 18 carbon atoms, octylphosphonate (OP) and octadecylphosphonate (ODP). They reported that longer chain lengths increase the contact angle and

hydrophobicity of the surface. OTS also has long hydrocarbon chain, so it has higher contact angle comparing to other SAMS with shorter hydrocarbon chain. In addition, shorter chains are not as well packed.

3.7 Oscillator Circuit

The oscillator circuit is used to drive the quartz crystal during the vapor phase lubricant uptake and it needs to work well properly despite high variable stray capacitances due to long crystal leads and mounting arrangements. The pierce oscillator circuit is therefore selected. Its high frequency stability even at very low drive levels is another great advantage. The circuit diagram of the Pierce oscillator circuit is presented in figure 3.6. The circuit gives simultaneous readings for frequency and amplitude of oscillation of the experimental crystal. The signals were fed to the computer via GPIB connection. A labview program is also design in order to read frequency, amplitude of oscillation and and pressure of the system and do necessary computations.

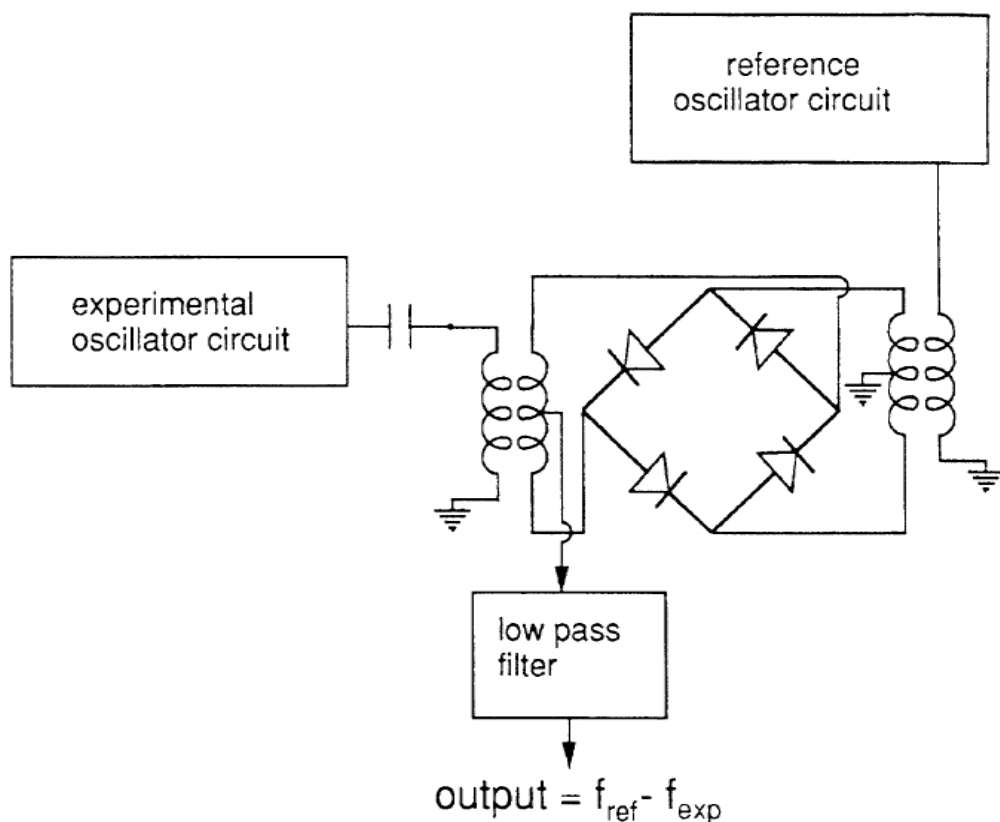


Figure 3.7 The diagram of mixer circuit which outputs the frequency and amplitude of the experimental crystal.

3.8 Sliding Friction Measurements

QCM is used as a probe for sliding friction. Krim and Widom developed this technique in 1986-1988, where they were able to show through acoustic impedance calculations, that if a film slips on the surface of QCM, its sliding friction could be related to the damping of the crystal's oscillation [43]. The acoustic impedance presented by the film to the substrate motion serves as the probe to the interfacial slippage. For this study, QCM is used to study the interfacial sliding and acoustic impedance of a viscous film, a 3-D gas and a film-vapor system are discussed.

3.8.1 Acoustic impedance of a viscous film

Consider a film of thickness d , with bulk density ρ_{3f} and bulk viscosity η_{3f} , lying on a flat, solid surface oscillating in plane with velocity $u = u_0 e^{-i\omega t}$. The motion of the solid surface will cause shear waves to propagate through the film. Taking the z -direction to be perpendicular to the solid surface, and the x -direction to be parallel to the motion of the surface, the film can be described by the Navier-Stokes equation for a viscous, incompressible fluid.

$$\rho_{3f} \frac{\partial v_x(z,t)}{\partial t} = \eta_{3f} \frac{\partial^2 v_x(z,t)}{\partial z^2} \quad (3.8)$$

In the equation $v_x(z,t)$ is the component of the film velocity in the direction of the motion of the solid surface. (From now on, the subscripts 2 and 3 will refer to surface and bulk values respectively, while f and v will refer to the film and vapor phases.) Assuming that the film does not slip on the solid surface and that its upper surface is free to move without any resistive force, the solution of the problem, for frequency f , is given by:

$$v_x(z,t) = u(t) \frac{\cos k(d-z)}{\cos(kx)} \quad (3.9)$$

where the dispersion relation is given by $k = (1+i) \sqrt{(\omega\rho/2\eta)}$. From the stress tensor component $\sigma_{zy} = \eta \left(\frac{\partial v_x}{\partial z} \right)_{z=0}$, one obtains the acoustic impedance, $Z = \frac{\sigma_{zy}}{v}$, presented by the film to the motion of the solid plane as:

$$Z_f = R_f - iX_f = \eta_{3f} k \tan(kd) \quad , \quad \text{where } k^2 = i \frac{\omega\rho_{3f}}{\eta_{3f}} \quad (3.10)$$

The resistive component R is proportional to the energy dissipation, while the reactive component X is proportional to the inertia of the oscillator.

Stockbridge has shown that the total frequency and quality factor shifts of the QCM are related to the total impedance presented to it by the relation [36]:

$$\delta\left(\frac{1}{Q}\right) = \frac{4R_{tot}}{\omega\rho_q t_q} \quad \text{and} \quad \delta(\omega) = \frac{2X_{tot}}{\rho_q t_q} \quad (3.11)$$

where ρ_q and t_q are the density and thickness of the quartz crystal respectively. These equations assume, as explained above, exposure of both electrodes of the crystal to the mass deposited. Of course, if only one side is exposed, the right hand side of the equations must be divided by 2. For very thin films, s , such that $|kd| \ll 1$, the dissipative part of equation 2.10 vanishes and the acoustic impedance reduces to:

$$Z_f = -i X_f = -i\omega\rho_{3f}d = -i\omega\rho_{2f}, \quad |kd| \ll 1$$

Substituting this result into equation 3.11 leads to Sauerbrey's result for the mass-frequency relationship given by equation 3.4.

3.8.2 Acoustic Impedance of a 3-D Gas

When the QCM is brought from vacuum to a gaseous environment, the acoustic impedance presented to the oscillator has contributions from the shear impedance of the gas, and mass uptake if gas adsorption occurs. Consider first the case when there is no adsorption. The acoustic impedance of a purely viscous gas (with bulk density η_{3v} and bulk viscosity η_{3v}) to shear wave propagation is given by the below equation [37].

$$Z_v = R_v - i X_v = (1-i)\sqrt{(\pi\rho_{3v}\eta_{3v}f)} \quad (3.12)$$

The reactive loading of the gas is equivalent to an increase in inertia of the oscillator

and leads to frequency shifts which could be calculated by substituting equation 3.12 into equation 3.11:

$$\frac{\delta f}{f_0} = \frac{\sqrt{\pi\rho_{3v}\eta_{3v}f}}{2\pi\rho_q v_q} \quad (3.13)$$

At low pressures, the relaxation time, τ_r , of the gas particles after collision with the vibrating crystal becomes commensurate with the period of oscillation. The gas therefore is no longer a simple viscous fluid but must be regarded as a viscoelastic fluid. Its viscosity becomes a function of frequency according to [38]

$$\eta_{3v}^* = \frac{\eta_{3v}}{1+i\omega\tau_r} \quad (3.14)$$

The acoustic impedance Z_v^* of the viscoelastic gas is then given by [33]

$$Z_v^* = R_v^* - i X_v^* \quad (3.15)$$

where

$$R_v^* = \sqrt{\pi\rho_{3v}\eta_{3v}f} \sqrt{\frac{\omega\tau_r}{1+(\omega\tau_r)^2} \left(\sqrt{1 + \frac{1}{(\omega\tau_r)^2}} + 1 \right)}$$

$$X_v^* = \sqrt{\pi\rho_{3v}\eta_{3v}f} \sqrt{\frac{\omega\tau_r}{1+(\omega\tau_r)^2} \left(\sqrt{1 + \frac{1}{(\omega\tau_r)^2}} - 1 \right)}$$

For pressures above 300 Torr, $\omega\tau_r \ll 1$, the relaxation argument becomes unimportant and equation $Z_v^* = R_v^* - i X_v^*$ degenerates into the classical viscous impedance given by this expressions, $Z_v = R_v - i X_v = (1-i) \sqrt{(\pi\rho_{3v}\eta_{3v}f)}$

3.8.3 Acoustic Impedance of a Film-Vapor System

If the gas adsorbs on the crystal under equilibrium conditions, the shear waves generated by the oscillator will diffuse away from the electrodes, through the film, and into the viscous gas. The acoustic impedance at the film-substrate boundary will therefore have contributions from both the adsorbed film and the 3-D vapor. Assuming there is no slippage at the film-substrate boundary, the acoustic impedance is given by:

$$Z_{fv} = Z_{3f} \tanh(\psi + \gamma d) \quad (3.16)$$

where,

$$\tanh(\Psi) = \frac{Z_{3v}}{Z_{3f}}$$

$$Z_{3v} = (1-i)(\pi\rho_{3v}\eta_{3v}f)^{\frac{1}{2}}$$

$$Z_{3f} = (1-i)(\pi\rho_{3f}\eta_{3f}f)^{\frac{1}{2}}$$

$$\gamma = Z_{3v} = (1-i)\left(\frac{\rho_{3f}\omega}{2\eta_{3f}}\right)^{\frac{1}{2}}$$

If the adsorbed film is sufficiently thin such that $|kd| \ll 1$, then the acoustic impedance reduces to:

$$Z_{fv} = -i\omega\rho_{2f}\left(1 - \left(\frac{Z_{3v}}{Z_{3f}}\right)^2\right) + Z_{3v}, \quad |kd| \ll 1, \quad (3.17)$$

Since the acoustic mismatch factor $1 - \left(\frac{Z_{3v}}{Z_{3f}}\right)^2$ is close to unity in most cases, the

above equation can be simplified to

$$Z_{fv} = -i \omega \rho_{2f} + Z_{3v} = Z_f + Z_v \quad (3.18)$$

The damping effects of the film and the gas vapor on the oscillator can therefore be separated and the frequency and quality factor shifts can be rewritten as:

$$\begin{aligned} \delta(\omega) &= \delta(\omega)_f + \delta(\omega)_v = \frac{X_f}{\rho_q t_q} + \frac{X_v}{\rho_q t_q} \\ \delta\left(\frac{1}{Q}\right) &= \delta\left(\frac{1}{Q}\right)_f + \delta\left(\frac{1}{Q}\right)_v = 0 + \left(\frac{R_v}{\omega \rho_q t_q}\right) \end{aligned} \quad (3.19)$$

3.9 Damping Due to Interfacial Slippage

The film impedance given in equation 3.18 assumes the 'no-slip' condition. Bruschi and Mistura calculated the effect of film slippage on the mechanical impedance presented to the QCM [39]. If the film slips on the surface of the electrodes, energy dissipation due to interfacial friction will introduce additional impedance $\frac{1}{\eta_2}$ in parallel to the 'no-slip' impedance of the film given in equation 3.18. We can write the total acoustic impedance as:

$$\frac{1}{Z_{total}} = \frac{1}{\eta_2} + \frac{1}{Z_{fv}} \quad (3.20)$$

Solving for the dissipative and reactive terms gives [3.11]:

$$\begin{aligned} \frac{X_{tot}}{R_{tot}^2 + X_{tot}^2} &= \frac{\omega \rho_2 + X_v}{R_v^2 + (\omega \rho_2 + X_v)^2} \\ \frac{R_{tot}}{R_{tot}^2 + X_{tot}^2} &= \frac{R_v}{R_v^2 + (\omega \rho_2 + X_v)^2} + \frac{1}{\eta_2} \end{aligned} \quad (3.21)$$

Slip time τ is calculated by solving for η_2 from above equations together with below equation:

$$\tau = \frac{\rho_{2f}}{\eta_2} \quad (3.22)$$

The slip time characterizes the decay of the total film momentum with respect to the substrate. It is a direct measure of how much slippage occurs at the film-substrate boundary. Note that it is an average over all the particles in the film, since not all of them are slipping in the same direction at a given time.

We can calculate the total dissipation R_{tot} and total reactance X_{tot} using the change in inverse quality factor and the change in frequency shift in equation 3.11. Then, using equation 3.22, we can calculate the interfacial slippage and the slip time, τ . Therefore, the slip time can be determined from frequency and quality factor measurements of the QCM.

Bruschi and Mistura's approach is a small correction to the earlier efforts of Krim and Widom [40]. Instead of equation 3.20, Krim and Widom used the following relationship:

$$Z_{total} = Z_v + \frac{Z_f \eta_2}{Z_f + \eta_2}$$

In the limit of low vapor density, the approaches of Bruschi and Mistura vs. Krim and Widom give the same result. As the vapor density increases, the Bruschi and Mistura approach gives a small correction (10% - 15%) to the Krim and Widom approach [41].

3.10 Experimental Determination of Quality Factor Q

Measurement of interfacial slippage requires simultaneous recording of both quality factor shifts and resonance frequency shifts. The QCM can be described as a damped driven harmonic oscillator. Its equation of motion is written as:

$$m \frac{d^2x}{dt^2} + b \frac{dx}{dt} + kx = F_o \cos t(\omega t) \quad (3.23)$$

where m is the total mass of the crystal and film, c is the damping constant and $\sqrt{\frac{k}{m}}$ the natural frequency of the crystal. The solution of equation 3.23 is $x=A\cos(\omega t - \phi)$.

Substitute this solution into equation 2.24 one obtains the expression for the amplitude as:

$$A(\omega) = \left(\frac{F_o}{((k - m\omega^2)^2 + c^2\omega^2)^{\frac{1}{2}}} \right) \quad (3.24)$$

and the phase angle:

$$\phi = \arctan\left(\frac{c\omega}{k - m\omega^2}\right) \quad (3.25)$$

Using the following relations:

$$\omega_o = \sqrt{\frac{k}{m}} \quad \text{and} \quad Q = \frac{m\omega_o}{c}$$

The amplitude $A(\omega)$ can be rewritten as:

$$A(\omega) = \left(\frac{\frac{F_o}{m}}{((\omega_o^2 - \omega^2)^2 + (\frac{\omega_o\omega}{Q})^2)^{\frac{1}{2}}} \right) \quad (3.26)$$

Approximately, $\omega \cong \omega_o$ since QCM is driven at its resonance frequency. The amplitude equation is simplified to:

$$A(\omega_o) \cong \frac{F_o}{m} \frac{Q}{\omega_o^2} \quad (3.27)$$

The variation of the amplitude with both frequency and quality factor are then given by equation 3.28.

$$\frac{\partial\left(\frac{1}{A}\right)}{\partial\left(\frac{1}{Q}\right)} = \frac{m}{F_o} \omega_0^2$$

$$\frac{\partial\left(\frac{1}{A}\right)}{\partial\omega} = \frac{2m}{F_o} \frac{2\omega_0}{Q} \quad (3.28)$$

Substituting the experimental values of $\omega \cong 10^8$ Hz and $Q \cong 10^5$,

$$\frac{\partial\left(\frac{1}{A}\right)}{\partial\left(\frac{1}{Q}\right)} \cong 10^{13} \frac{\partial\left(\frac{1}{A}\right)}{\partial\omega} \quad (3.29)$$

The above equation is independent of frequency changes and the change in inverse amplitude is proportional to the change in inverse quality factor. Therefore, amplitude changes can be used to monitor changes in the quality factor directly. From this quality factor and frequency measurement, slip time τ can be calculated using the below equation:

$$\tau = \frac{\delta\left(\frac{1}{Q}\right)_f}{4\pi(\delta f)_f} \quad (3.30)$$

In the equation, τ is a characteristic time for the object's velocity to decay to 1/e of its initial velocity. Another way to look at this characteristic time τ is by considering the body moving through viscous fluids. Viscous friction being parameterized at low velocities is shown by the following equation. Here v is the velocity of the object through the fluid, m is the object's mass.

$$F = \frac{mv}{\tau} \quad (3.31)$$

3.11 Auger Electron Spectroscopy (AES)

In this study, Auger Electron Spectroscopy is used to do the surface analysis on the samples. Auger Electron Spectroscopy (AES) is well-established techniques for surface analysis. It was first suggested by J. J. Lander in 1953 [42] and in 1967 Larry Harris demonstrated the use of differentiation for enhancing the Auger signals. The first paper about Auger electron spectroscopy (AES) was then published in 1968. Auger Electron Spectroscopy uses a primary electron beam to probe the surface of a solid material. Secondary electrons, which can be emitted as a result of the Auger process, are analyzed and their kinetic energy is determined. When analyzed as a function of energy, the peak positions are used to identify the elements and the chemical states present. All elements in the periodic table, except hydrogen and helium, can be detected. Since Auger electrons can only escape from the top 2-20 atomic layers of a solid surface at their characteristic energy, this effect makes AES an extremely surface sensitive technique.

The basic Auger process starts with removal of an inner shell atomic electron to form a vacancy. A second atomic electron from a higher shell fills the inner shell vacancy. The energy released in this process caused emission of a third, the Auger electron. The Auger electron energies are characteristic of the target elements. Therefore, Auger electron spectroscopy identifies elemental compositions of surfaces by measuring the energies of ejected Auger electrons. The kinetic energy of the KLL auger electron is given as:

$$\text{K.E.} \sim (E_K - E_L) - W$$

W is the escape energy of the electron from level L . The above relation is approximate since the interactions between the two final-state holes are not included, which is rather a small correction.

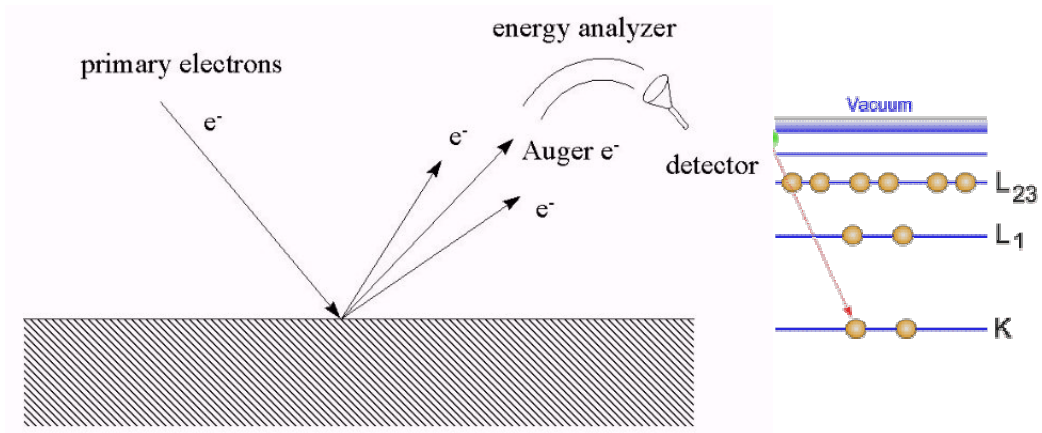


Figure 3.8 The three steps of the Auger process leading to ejection of an Auger electron. As shown in the left figure, the green incident electron is colliding with $1s$ shell electron. The second atomic electron from a higher $2s$ shell fills the inner shell vacancy. This generates a radiation which causes an Auger electron to be ejected.

CHAPTER 4

EXPERIMENTAL APPARATUS AND PROCEDURE

This chapter will describe in detail how the QCM technique is used to measure friction, and the experimental apparatus with which I acquired my data. The vapor phase lubricant studies described in this work require high vacuum conditions to ensure sample quality and integrity and also purity of the vapor phase lubricants studied. Nearly all data taken to prepare this dissertation was acquired using QCM in UHV chamber as described here.

4.1 Experimental Hardware

In Figure 4.1, the vacuum system is shown. The main chamber houses the experimental quartz crystal and the vapor phase lubricant source. It is also connected to pressure gauges, N₂ gas tank and gas container. The gas dosing area is separated from the main chamber by the leak valve. The pressure of main chamber is held at high vacuum by an ion pump. A turbo pump backed by a sorption pump brings the pressure down to $\sim 10^{-5}$ Torr before turning on the ion pump.

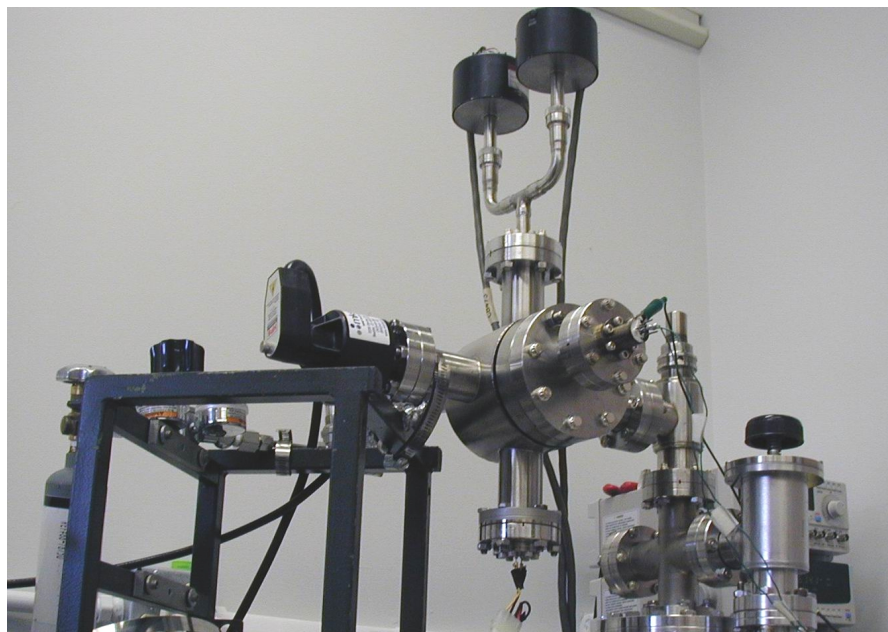


Figure 4.1 Show the vacuum system for QCM experiment

The pressure in these experiments is monitored by multiple pressure gauges. One high pressure gauge measures the chamber pressure below 1 mTorr. Two Baratron pressure gauges are used to measure the pressure between 1 mTorr to 1000 Torr. A digital multimeter having GPIB capability reads pressure from Baratron pressure gauges is interfaced with a computer. During nitrogen calibration runs, the pressure of the chamber is recorded with Labview program via GPIB connection. The program also records frequency and amplitude of the crystal in real-time during vapor phase lubricant uptakes. As shown in Fig. 4.3, the QCM crystal is fitted into a pair of metal spring clips, which are mounted on an insulated base. Spring clips ensure good electrical connection between the crystal tabs and the mount posts. Signals from QCM crystal are sent to pierce oscillator circuit via electrical feedthroughs and to the computer. The Pierce oscillator circuit is powered by a DC power supply at 10 V. The circuit drives the QCM at its resonance frequency with great stability. In

equilibrium conditions, the crystal can be held at a constant frequency of 5 MHz with a drift of +/- 1 Hz for several hours.

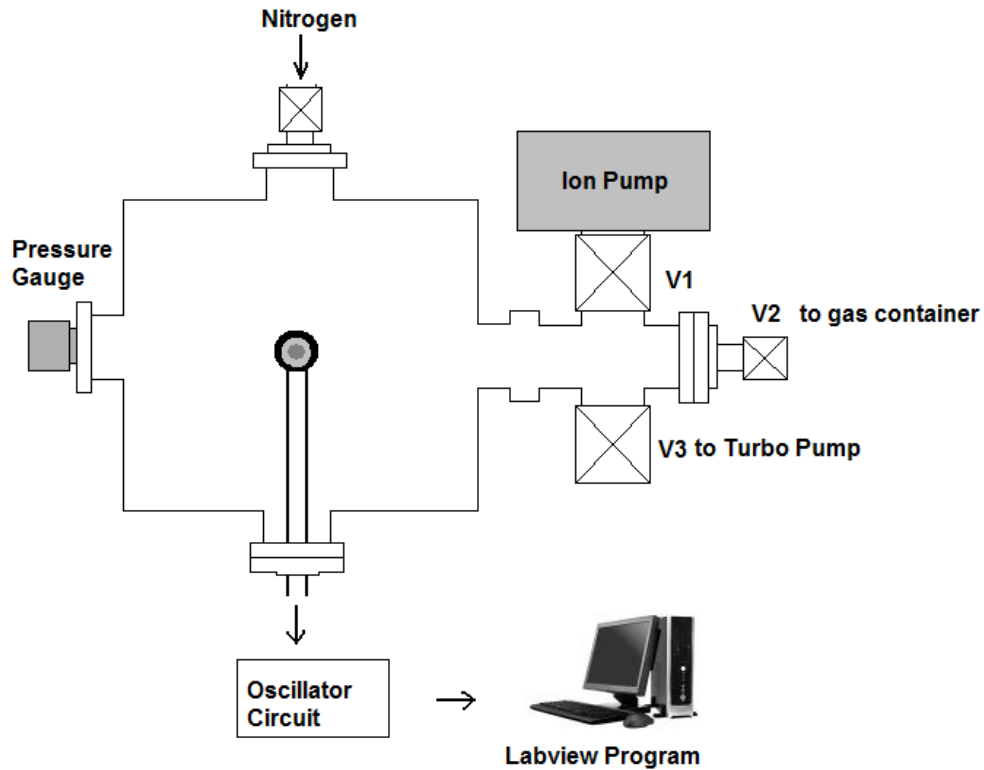


Figure 4.2 A diagram of experimental setup (top view). An experimental crystal is vertically placed in the middle.

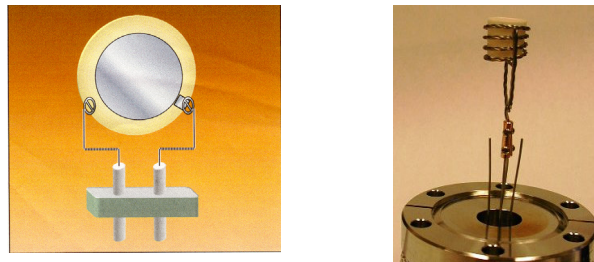


Figure 4.3 a) The QCM crystal is fitted into a pair of metal spring clips, which are mounted on an insulated base. Spring clips ensure good electrical connection between the crystal tabs and the mount posts.

b) Show the ceramic crucible containing the vapor phase lubricant is wrapped around with tungsten coil.

4.2 Experimental Procedure

The crystal is put in the experimental chamber which is then pumped down to the base pressure of 2×10^{-7} Torr. The valve to the ion pump (V1) is close during vapor phase lubricant uptake. After closing the valve, Labview program is started. However, the uptake will not start until ten minutes later. This is because we want to see if there is no frequency shift before vapor phase lubricant starts evaporate. The power supply is turned on with current of 3A. The power supply is then turned off after 60 minutes. The Labview program record frequency and amplitude of the crystal in real-time and record the pressure during nitrogen calibration runs. A wire thermocouple is also used to record the temperature of the lubricant with the Labview program via GPIB connection.

4.2.1 Sample Preparation

Quartz crystals go through the cleaning procedure which is adopted with modification from previous work by Brzoska et al., [44]: (1) thoroughly washing the samples with running water, (2) rinsing with DI water, (3) immersion in 0.05 M NaOH solution for approximately 30 min, (4) a UV/O₃ treatment for 30 minutes.

After cleaning, the Si crystals were sent directly to a vacuum chamber for TCP or TBPP uptake measurements, or alternately immersed in a solution of hexadecane and chloroform (4:1 by volume), whose temperature was regulated to 20.00 ± 0.05 C. Chloroform acts as a cosolvent to increase the solubility of chlorine head. OTS was then injected into the solution and allowed to assemble on the samples. After removal from the OTS solution, the crystals were rinsed with chloroform to remove excess OTS so leave in place a monolayer. The immersion time for OTS monolayer preparation varies among

different research groups. Intervals of 1 minute and up to 1 hour had been employed, but usually 10 to 15 minutes [45, 46]. The quality of monolayer film is not much different for immersion time over 15 minutes.

The substrate must be prepared carefully. Water must be removed from the surface. After drying, successive cleaning steps are performed. During the cleaning process, the substrate surface must be hydroxylated to create the necessary deposition sites on the surface. Hydroxylation is usually done via immersion in piranha solution ($\text{H}_2\text{O}_2:\text{H}_2\text{SO}_4$) [46], or exposure to UV/ozone [47].

4.2.2 Calibration

As we discussed in the preceding section, the circuit output is proportional to the amplitude of the experimental crystal. We have shown that the shift of the reciprocal amplitude ($1/A$) is directly proportional to the shift in the dissipation factor ($1/Q$), for example,

$$\delta\left(\frac{1}{Q}\right) = C \delta\left(\frac{1}{A}\right)$$

Finding the constant C is what we call calibration of our data taking setup. Admitting a non-adsorbing gas with known acoustic impedance as a function of pressure into the experimental chamber. Plotting changes of the reciprocal of the amplitude versus changes in the dissipation factor, which is proportional to changes in acoustic impedance, will yield the calibration constant, C .

In calculating the slip time, the program analysis is automatically subtracting the contribution to the acoustic resistance due to TCP gas pressure from the total acoustic

resistance. In fact the TCP vapor pressure is very small, therefore this correction is really negligible in our study.

CHAPTER 5

EFFECT OF EXTERNAL GAS TO WATER FILM LAYER

5.1 Experimental Procedure

The same routine checks were performed to assure stable frequency and amplitude of oscillation signals. The gold quartz crystal is put in the experimental vacuum chamber and was connected to pierce oscillator circuit via electrical feed through. The routine nitrogen calibration was performed. Then the main vacuum chamber is pumped down to base pressure of 4×10^{-5} Torr and ready for uptake measurement. Three systems were to be studied:

- i) Water vapor uptake measurement in Vacuum
- ii) Water vapor uptake measurement in Nitrogen gas environment
- iii) Water vapor uptake measurement in Argon gas environment.

To carry out the water vapor uptake measurement, all valves are closed and Labview program was run. Simultaneous data of frequency and amplitude of the QCM oscillation were collected. After ten minutes, the valve V2 is slowly opened to let the water vapor into the main chamber (see figure 5.1). Stop the run when the pressure is about 10 Torr. Slip time is then calculated.

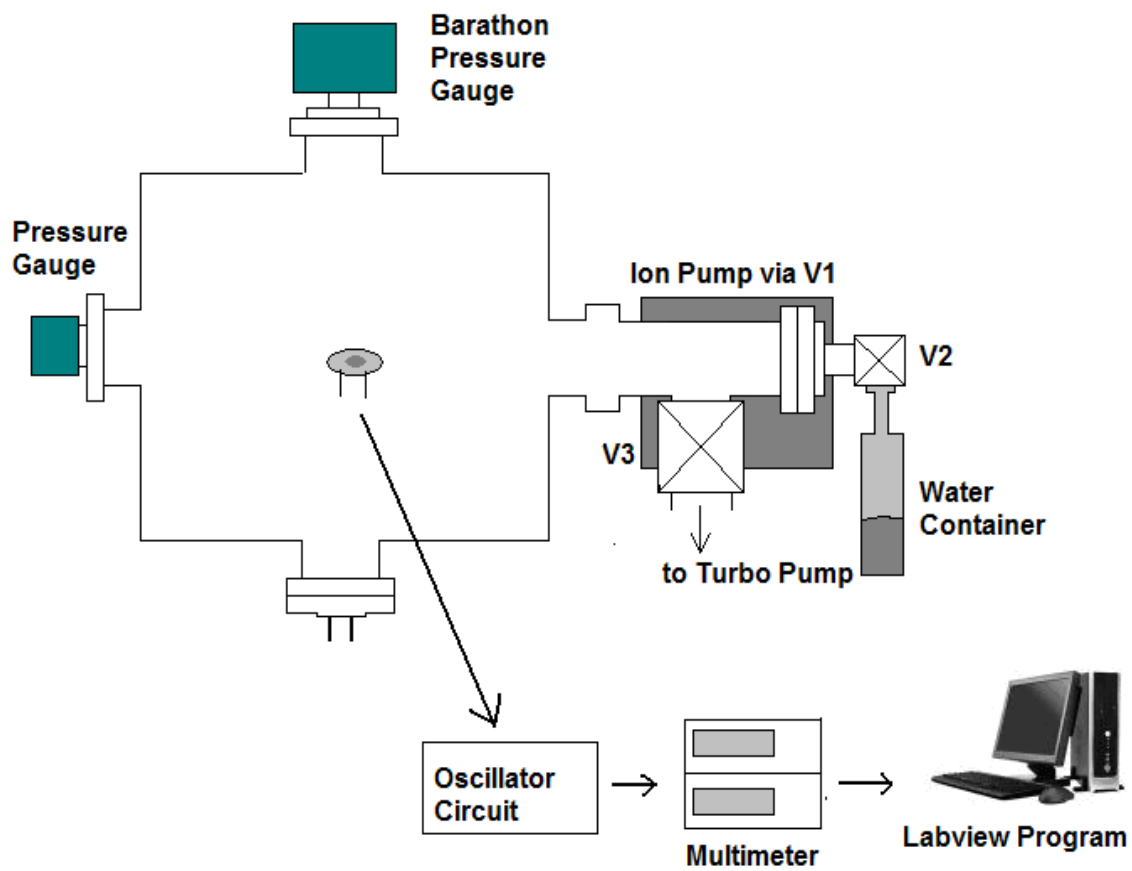


Figure 5.1 The side view of the experimental setup. The water vapor container is attached to valve V2.

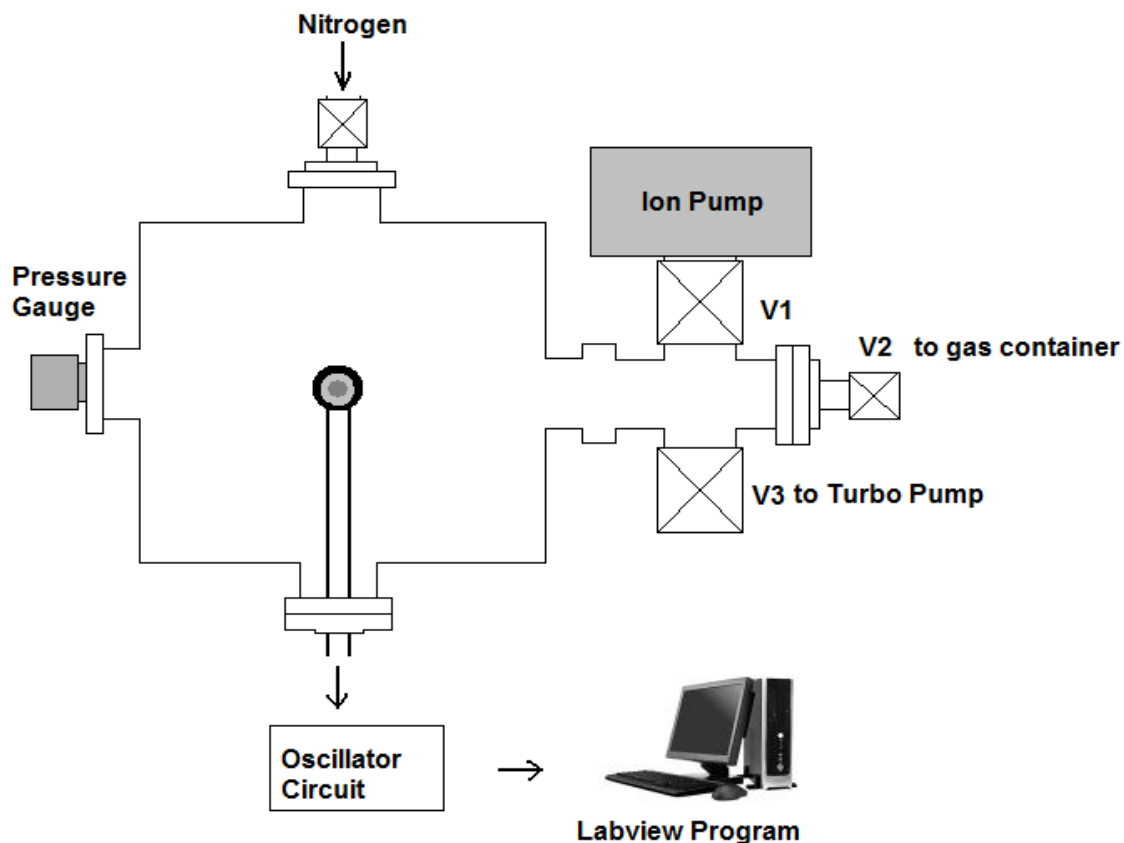


Figure 5.2 A schematic diagram of experimental setup (top view). An experimental crystal is horizontally placed in the middle.

After previous experimental run, the vacuum chamber must be baked for at least 24 hours to get rid of water adsorbed at the chamber wall. Then the new crystal was placed and same routine checks were performed to assure stable frequency and amplitude of oscillation signals. After a regular calibration was performed, the main vacuum chamber is pumped down to the base pressure. To study the effect of environmental gas to the water film layer, the gas (N_2 or Ar) is leaked into the main vacuum chamber via the valve V4 (see figure 4.1). Then the water vapor uptake experiment was performed. The Labview program records frequency and amplitude of the crystal in real-time and record the pressure during calibration runs. Slip time was then calculated.

5.2 Result and Discussion

5.2.1 Water Vapor Uptake

Figure 5.3 shows the frequency shift vs time and the frequency shift is 11.4 Hz after 40 minutes of water vapor uptake. From the observation, the small change in quality factor indicates little slip of water film as shown in the bottom graph.

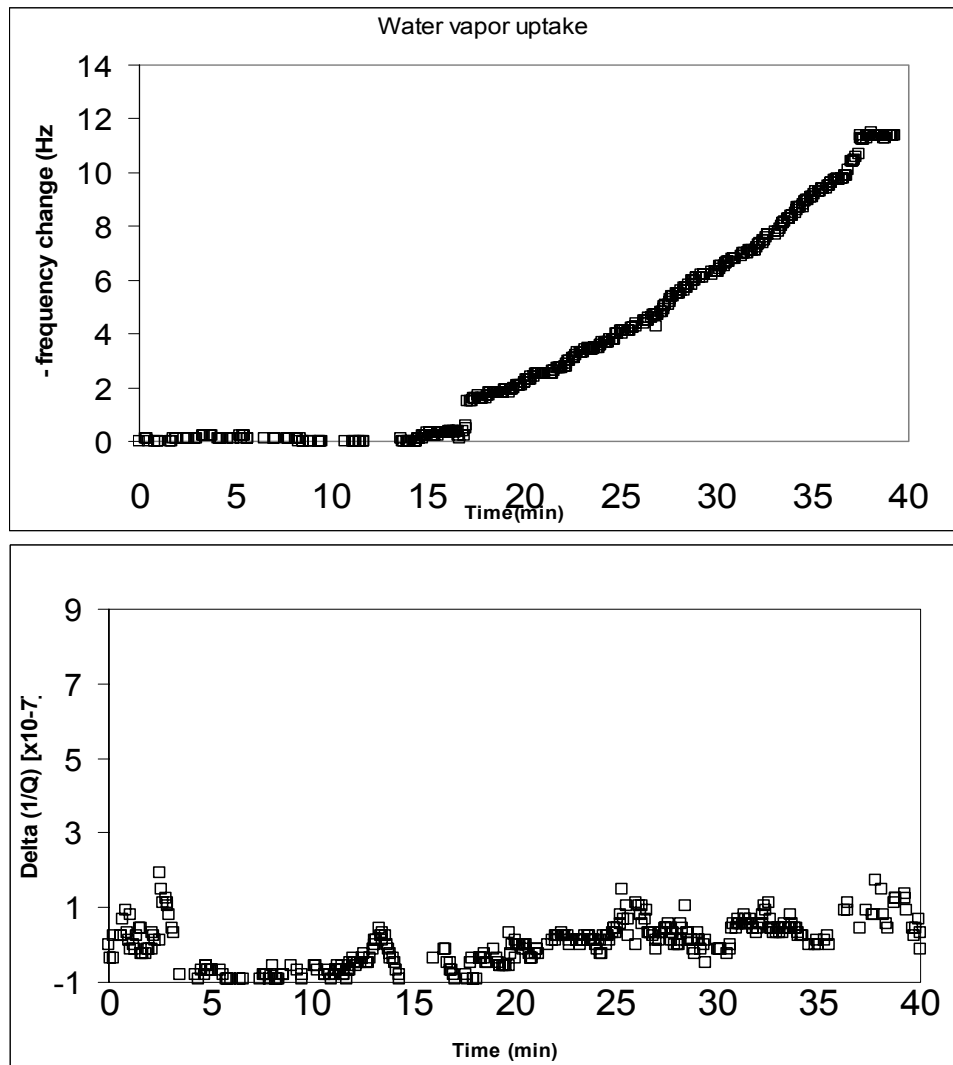


Fig 5.3 Shows frequency data (top) and Q^{-1} shift data (bottom) for water vapor uptake onto quartz crystal surface in vacuum (Adsorption data file: 01062006b.txt with N2 calibration data: 01062006a.txt).

5.2.2 Water Vapor Uptake in N₂ gas (or Ar)

The N₂ gas (or Ar gas) was leaked into the vacuum chamber before starting the water vapor uptake. We observed no change in frequency and quality factor during the gas uptake (N₂ or Ar). Then water vapor adsorption was carried out.

Figure 5.4 show the results of the water film adsorption with different type of surrounding gas. Slip times were calculated for each system with the same thickness of about 14.04 ng/cm². The slip time of water vapor film uptake in vacuum is 0.23 ns. With the present of Ar gas (or N₂ gas), the calculated slip time is 4.22 ns (or 20.37 ns).

The result shows that water vapor film slips more when nitrogen is present and the environmental gas definitely has an impact on the slip time of water vapor film. The film slips very much less when there is no environmental gas. In the next section, we will discuss how dissolved gas increases the hydrophobicity of water, which has the impact on the slip time and sliding friction of water film.

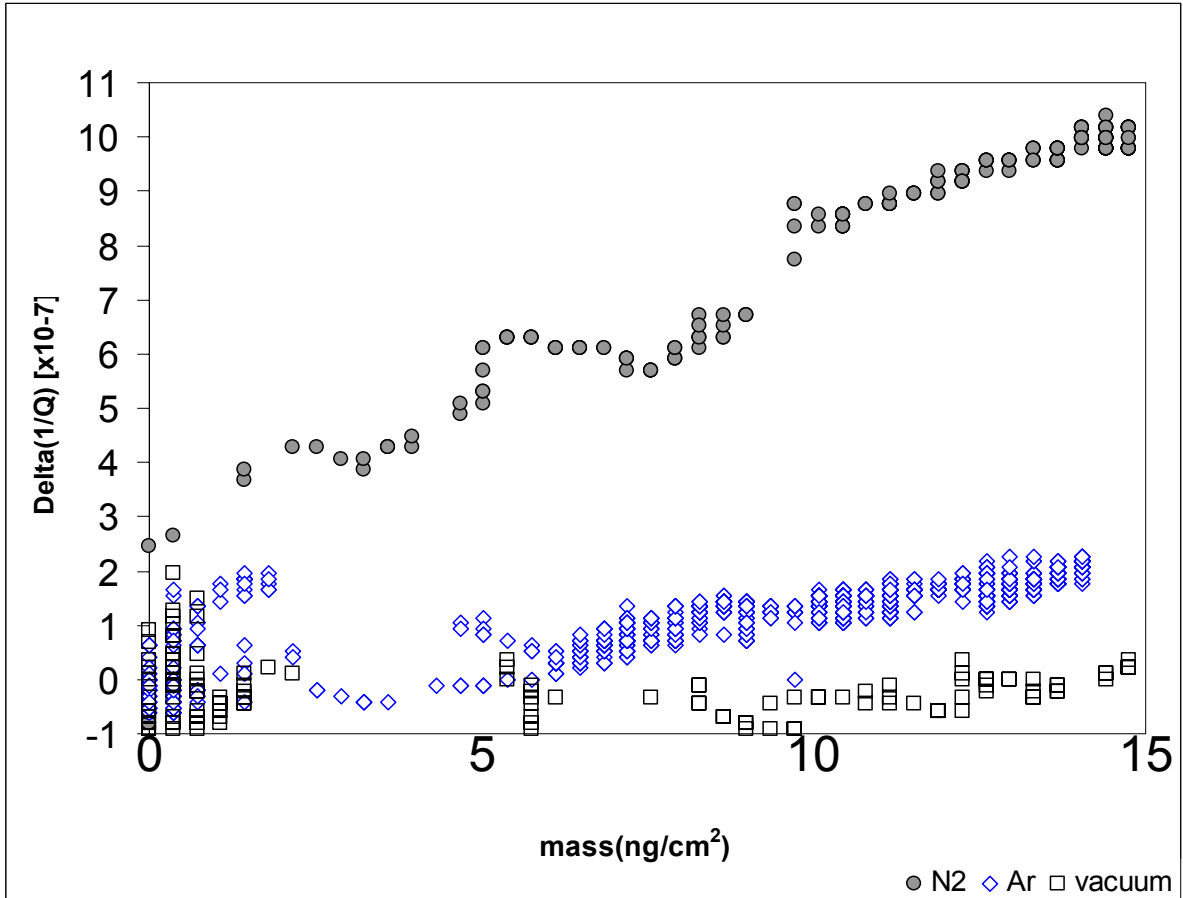


Figure 5.4 The plot of Q^{-1} shift vs mass deposited data for water vapor uptake onto quartz crystal surface in vacuum (open square: Adsorption data file:01062006b.txt with N_2 calibration data: 01062006a.txt), with the present of Nitrogen (filled circles: Adsorption data file:01182006b.txt with N_2 calibration data: 01182006a.txt) or with Argon gas (open diamonds: Adsorption data file:02072006b.txt with Ar calibration data: 02072006a.txt).

5.3 Discussion

As shown in Fig 5.4, the change in inverse of quality factor does in fact depend on the nature of the surrounding gas. In this section we will investigate what is causing the slip time to be different for different gas environments. We note that Granick et. al also observed the impact of the surrounding gas on the slippage and stated that argon segregated to the solid walls, creating a low-viscosity boundary layer, that enabled the flow of fluid past that surface. Presumably, the amount of segregation is a materials property of the fluid, the chemical makeup of the surface, and the chemical identity of the dissolved gas [5].

In this study, Nitrogen and Argon gas were used, both of which have low solubility in water. The gas having lowest solubility in water may have difficulty in segregating to the surface. It could be possible that small gas bubbles of nitrogen were formed across the surface and helps the water film to slip more, as shown in Fig 5.4. The mechanism was first discovered by Vinogradova [47] and recently expanded on by de Gennes, who conjectured that shear may induce nucleation of vapor bubbles. Once the nucleation barrier is exceeded the bubbles grow to cover the surface, the liquid is flowing over the thin gas film instead of the substrate[48]. Ruckenstein and Rajora [10] also suggested that it is possible that entrained or soluble gases in the flowing liquid may increase fluid slip by forming a gap between the liquid and the wall, thereby increasing the slip length β . However, the type of surrounding gas strongly influences the slippage, as shown in this study. As reported in literature, the friction of MEMS surface is reduced when MEMS operates with alcohol surrounding [50].

TABLE 5.1 Solubility coefficients of nitrogen and argon in water at room temperature.

Type of Gas	Solubility in water (Vol/Vol)
N ₂	0.0234
Ar	0.0537

This solubility coefficient assists in explaining how gas molecules react to the water film layer. So far we are under the assumption that there is a possibility that gas bubbles or a thin gas film could exist on the surface between water film layer and solid surface. Let's take a look at how water vapors react to gas molecules covering the solid surface. From experimental data, we can take a look at how long water vapor adsorption took in order to form one monolayer of water film. 10 minutes, or 600 seconds are required to form one monolayer of water film on gold surface. In a different gas surrounding, we expect that each gas will have a different sticking coefficient. In the case of water vapor adsorption in vacuum, the water molecules stick readily to the substrate. This is confirmed by a very small change in inverse quality factor shown in Fig. 5.3 and 5.4. Therefore, we can find where a monolayer (or 15 ng/cm^2) of water vapor is formed and normalize to the sticking-rate ratio of adsorption in vacuum. As a result, the sticking-rate ratios of N₂ and Ar are calculated to be 0.45 and 0.13, accordingly.

TABLE 5.2 The sticking-rate coefficients normalized to the vacuum system.

Type of surrounding gas	Time to obtain a monolayer of water vapor film (sec)	Sticking-rate ratio (Normalization to vacuum)
Vacuum	600	1.0*
N ₂	1320	0.45
Ar	4800	0.13

*Set equal to one and normalized to the system in vacuum.

This explains why water vapor uptake in Ar surrounding has a smaller change in inverse quality factor: in other words, water vapor film slips less in argon environment (see Figure 5.4). In argon gas surrounding, it does take a longer time to get a monolayer of water vapor film as shown in the table 5.2. This could be explained by the higher solubility coefficient in water for argon. During the water vapor adsorption, argon molecules in the chamber may dissolve in water layer. As a result, it takes longer time to form a monolayer of water film as observed in experimental data in Figure 5.4. In contrast, it takes less time to form a monolayer when the surrounding gas is nitrogen, which has a lower solubility coefficient in water.

Another way to view what is happening at the interface between water and the substrate is to consider the relationship between surface tension and hydrophobicity of water with different dissolved gas.

It is known that the surface tension is responsible for the shape of liquid droplets. The surface tension of water provides the necessary wall tension for the formation of bubbles with water. Droplets of water tend to be pulled into a spherical shape by the cohesive forces

of the surface layer. The spherical shape also minimizes the necessary wall tension of the surface layer according to Laplace's law [51].

The molecules on the surface frontiers have water on one side and something else on the other: for example, N₂ or Ar molecules. Water molecules are not only attracted to other water molecules. If they are more strongly attracted to the molecules of another substance, that substance is said to be wetted, or hydrophilic and surface molecules tend to approach it. If they are less attracted, the substance is hydrophobic and surface molecules tend to shy away from it. The water-air surface meets another at an angle of contact θ . This angle is small for a hydrophilic surface, large for a hydrophobic surface. It is 90° if the attraction is the same as that of water itself. All of this is strongly affected by the purity of the surfaces involved.

In this study we use non polar gas molecule, such as a noble gas atom, Ar, to dissolve in water. The noble gas alone has no charge and therefore can not have a Coulomb interaction with the water molecules, only van der Waals interactions. Therefore, the effect of dissolved gas in water is primarily a consequence of changes in the clustering in the surrounding water rather than water-solute interactions. This is called hydrophobic effect which causes a reduction in density and an increase in the heat capacity [52]. The expanded network causes the density decrease whereas the ordered bonds must be bent on increasing the temperature, so affecting the heat capacity. There is also likely to be an overall reduction in volume due to more efficient solute packing density. This hydrophobic effect decreases with increased density as it is dependent on the presence of tetrahedrally-placed water molecules, which reduce in number under the distorting influence of pressure [53]. In other words, low-density water increases the interfacial energy of water. Doshi et. al used neutron

reflectivity technique to show that dissolved gasses reduce the surface density, and their removal of dissolved gasses increases the water density region back to where it was. Their result is shown in Table 5.3 (taken from ref. [54]). Neutrons are particularly useful in studies of buried solid-liquid interfaces because of their large penetration depth, angstrom resolution, and the remarkable contrast between hydrogenated and deuterated species. Their results are summarized in the below table. The smallest reduced water density region offset, defined by δ , was observed for a D₂O with Ar. The largest for was naturally aerated D₂O with mainly N₂ and O₂, where CO₂ fell in between (see Table 5.3). The dissolved gasses have the possibility to adsorb at the water interface [52]. However, they suggested that it is still not obvious why different gasses with comparable water solubility exhibit different adsorptions. Can it be because of the change in hydrophobicity of water?

Table 5.3 Results for neutron reflectivity performed on OTS against different water subphases [54].

Subphase	Combined average thickness (Å)	Reduced water density region Offset, $\delta \pm 0.5$ (Å)	Width of the error-function profile, σ , (Å)
Untreated (naturally aerated) D ₂ O			
(a)	34.8	11.3	3.6 ± 0.3
(b)	33.7	10.3	3.2 ± 0.5
(c)	31.0	7.6	3.4 ± 0.2
Ar D ₂ O	26.5	2.0	4.2 ± 0.3
CO ₂ D ₂ O	28.8	5.8	3.7 ± 0.8
Before degassing	31.0	7.6	3.4 ± 0.2
Vacuum degassed D ₂ O			
T = 0 hr	28.6	5.2	2.1 ± 0.2
T = 5 hr	29.1	5.7	2.9 ± 0.6
T = 18 hr	30.3	6.2	4.2 ± 0.1

Hydrophobicity of water may have an impact to the friction of water film sliding on a quartz crystal. Mentioned earlier, dissolving N_2 and O_2 gasses reduce the surface density more than dissolved CO_2 gas and much more than Ar [54]. Furthermore, low-density water increases the interfacial energy of water. Therefore, dissolved N_2 increases the interfacial energy of water which then increases the hydrophobicity of water film. Therefore, hydrophobicity of water can have an effect on the friction of water film (or slip time in our study).

Using extensive molecular dynamics simulations, two physicists, Barrat and Bocquet, shows interfacial slippage at the partially-wet surface can happen when the contact angle (or hydrophobicity of liquid) is large enough [4]. Their discovery explains the relationship between interfacial slippage and hydrophobicity of liquid. In our experimental data, we also observe interfacial slippage of water dissolving with N_2 and Ar as shown in Fig 5.4. The system in N_2 environment has higher slip time (or less friction). This can be explained that dissolved N_2 increases interfacial energy of water which then increases the hydrophobicity of water film. As a result, water with higher hydrophobicity (or larger contact angle) slips more at the substrate-water interface [4]. The system in Ar surrounding does not slip as much as the system in N_2 surrounding could be because of smaller reduced-water-density-region, which is resulting in smaller interfacial energy and smaller hydrophobicity. Here, our study has just shown that hydrophobicity of water in different type of surrounding gas has an effect on the slip time.



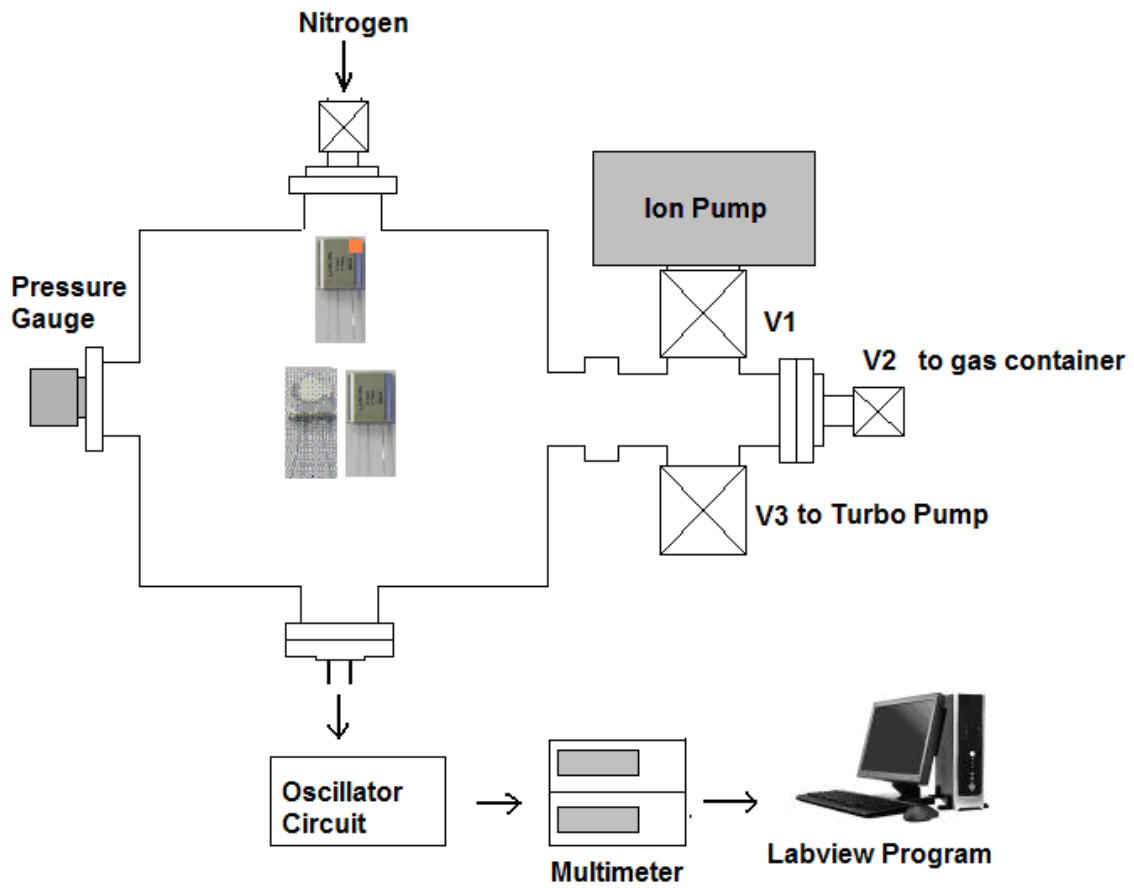
Figure 5.5 Illustrate the possible shape of water droplet in different dissolving gas surrounding. Hydrophobicity is increased in N_2 (left) and Ar (right) environment (not drawn to scale).

CHAPTER 6

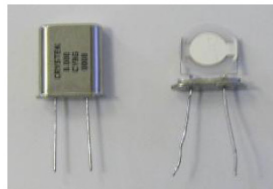
VAPOR PHASE LUBRICANT UPTAKES

6.1 Uptake of Lubricants on Ag Surfaces

Our preliminary study of vapor phase lubricant uptake on quartz crystals were carried out to determine whether the vapor phase lubricant could travel far enough deposit itself on the QCM crystal surface. This was conducted by uptaking the vapor phase lubricant on three 8 MHz Crystek Corp quartz crystals which were in the cans shown in figure 6.1(b). The crystal size is small enough to have three crystals in the main vacuum chamber for each experimental run. Some quartz crystal cans were removed as shown in figure 6.2(a). One crystal can was drilled to have a small hole at the edge of the can. Then they were placed in different orientation as shown in the figure below. The frequency shifts on all three QCM crystals indicate that vapor phase lubricants are able to find its way to deposit itself onto the QCM surfaces. This is important since this result confirms that vapor phase lubricant will be able to coat the MEMS surface even in the out-of-sight line.



(a)



(b)

Figure 6.1 (a) Schematic diagram of the vacuum setup and (b) how Crystek quartz crystals were placed in the vacuum chamber.

After sample preparation as described in previous chapter, a number of routine checks were performed to assure stable frequency and amplitude of oscillation signals. The crystal is put in the experimental vacuum chamber which is then pumped down to base pressure of 2×10^{-7} Torr. All valves are closed before starting the data-taking Labview program. During the uptake, the power supply is set to 3A. The crystal is connected externally to the Pierce oscillator circuit via the electrical feedthroughs. Simultaneous data of experimental chamber pressure, temperature, frequency and amplitude of the QCM oscillation were collected. Each run lasted approximately one hour.

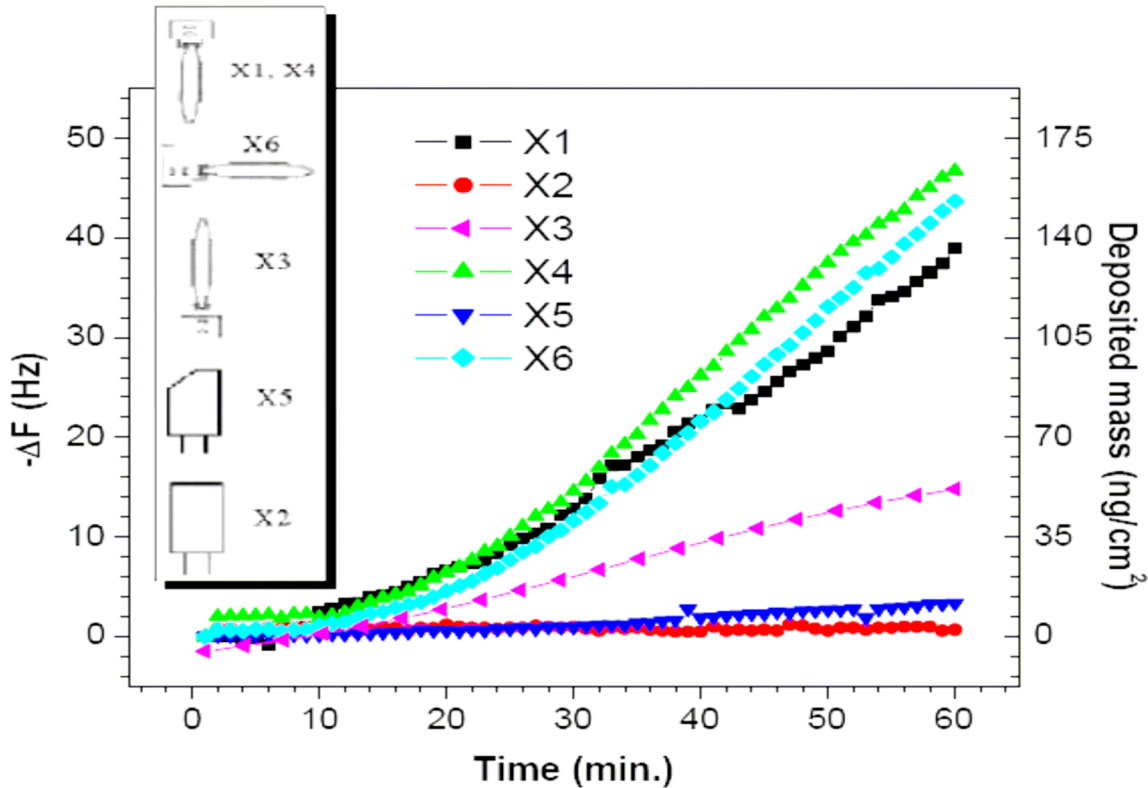


Figure 6.2 Frequency changes of the QCM of six crystals during the lubricant uptakes.

Figure 6.2 shows the results of the QCM uptake results. The plot combines six experimental runs. The analysis gives a fair picture about the nature of vapor phase lubricant.

Two of the crystals are used with their encapsulation removed, while the other is used with the can (encapsulation) to test frequency drifts due to temperature variations. All three crystals are placed in the vacuum chamber, above the crucible containing the lubricant, held by the tungsten heating wire. The experiment is conducted at room temperature.

Another set of experimental run is conducted. Three crystals are used and two crystals with their cans removed were placed right above the lubricant source. The third one with a hole on the edge of the can was placed away from the lubricant source.

X1 and X4 are the plots of crystals (Crystal 1 and 4) placed vertically down, right above the VPL source. These plots show that the pattern of uptake is approximately the same in both cases. The change in frequency in case of Crystal 1 is 38.98 Hz, and 46.75 Hz in case of Crystal 2. The mass deposited in these two cases are 134.60 ng/cm^2 and 161.42 ng/cm^2 respectively. X2 is the plot of the crystal, which was used to calibrate any temperature variations that might have caused the change in frequency during the experimental run. The plot shows that there were no such temperature variations.

X3 is the plot of the crystal placed vertical (facing up), away from the lubricant source in the vacuum chamber. This analysis is helpful in determining whether the vapor phase lubricant could travel far enough to deposit itself on the crystal 3. The plot shows a frequency shift of 14.812 Hz, and 51.14 ng/cm^2 of mass deposition, which is approximately half of that of crystal 1. X5 is the plot of the crystal, whose outer can was kept intact except for a small hole drilled at the edge of the can. This helped in knowing whether the vapor phase lubricant could make its way through the hole and deposit itself onto the crystal. The plot shows a frequency shift of 3.4 Hz, with a corresponding mass deposition of 11.74 ng/cm^2 . This shows that even though the mass adsorbed is less, the vapor phase lubricant did

deposit itself onto the quartz crystal. Plot X6 is that of crystal 6, which is placed horizontally, right above the lubricant source. As can be seen from Figure 6.2, this plot follows that of Crystals 1 and 4, proving that the vapor phase lubricant can actually move around the crystal and deposit itself onto the opposite electrode. The frequency shift in this case is 43.7 Hz and the mass deposited on this crystal is calculated as 150.896 ng/ cm².

This study helps understanding the way the MEMS devices ought to be positioned in order to obtain well-lubricated devices. It also confirms that vapor phase lubricant being delivered in gas phase can make its way and deposit itself onto the crystal surface.

6.2 Vapor phase lubricant uptakes on ozone-cleaned silicon oxide surfaces

From the previous study, it showed that the vapor phase lubricant traveled around the chamber and was able to deposit itself onto the crystal surface. In this section we studied the uptakes of two high-temperature vapor phase lubricants and how well they lubricated the silicon surfaces.

6.2.1 TCP and TBPP uptakes on amorphous silicon oxide surface

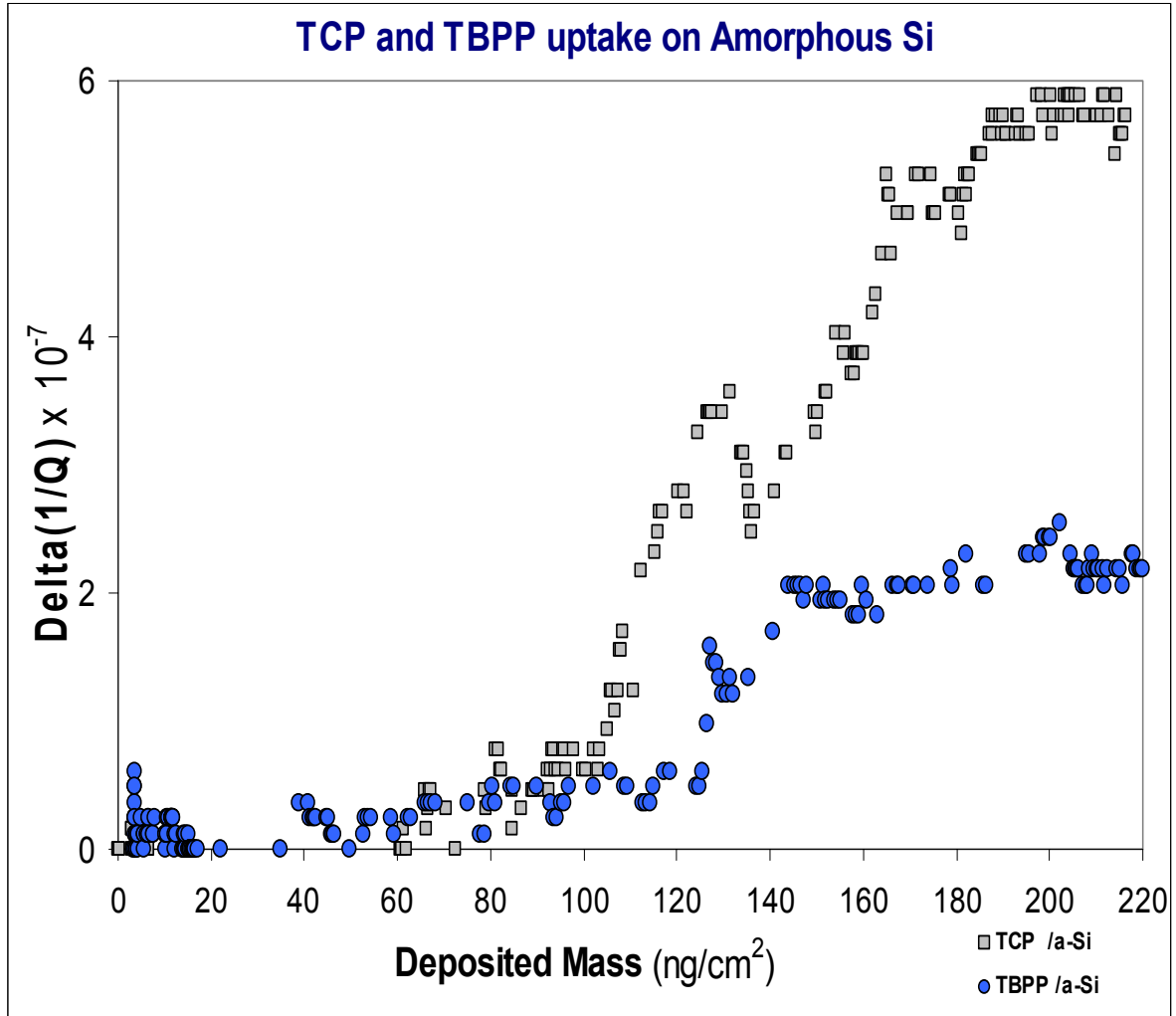


Figure 6.3 Deposited mass and Q^{-1} shift data for TCP uptake on amorphous silicon oxide surface (filled squares:) and TBPP uptake on amorphous silicon oxide surface (filled circles).

Adsorption of TCP and TBPP of amorphous silicon oxide surface

Figure 6.3 presents deposited mass and inverse quality factor shift data for vapor phase lubricant (TBPP and TCP) adsorption on ozone-cleaned amorphous silicon surface at room temperature. The frequency shift corresponding to one monolayer of TCP is about 10.6 Hz.

The uptake of both TCP and TBPP are similar, but we observe more slippage in the case of

TCP. The inverse quality factor data reveal that TCP slides readily on the cleaned silicon surface, characterized by slip times on the order of 0.9 ns. The slip time of TBPP on the same silicon surface is shorter (0.3ns). The results are summarized in the second column of Table 6.1.

6.2.2 TCP and TBPP uptakes on polycrystalline silicon oxide surface

Adsorption of TCP and TBPP on polycrystalline silicon oxide surface

Figure 6.4 presents deposited mass and inverse quality factor shift data for vapor phase lubricant (TBPP and TCP) adsorption on ozone-cleaned polycrystalline silicon room temperature. Although TBPP is not a pure material, a 'monolayer' of its constituents would result in a frequency shift on the same order as TCP. In contrast to TBPP, TCP uptake on the surface is substantial, with the equivalent of five monolayers of material adsorbing in one hour. TBPP uptake on is slightly limited, with three layers of material adsorbing after sixty minute's time.

The inverse quality factor data reveal that TBPP slides on the polycrystalline surface, characterized by slip times on the order of 0.25 ns. The slip time for TCP is shorter (0.14ns). The results are summarized in the first column of Table 6.1.

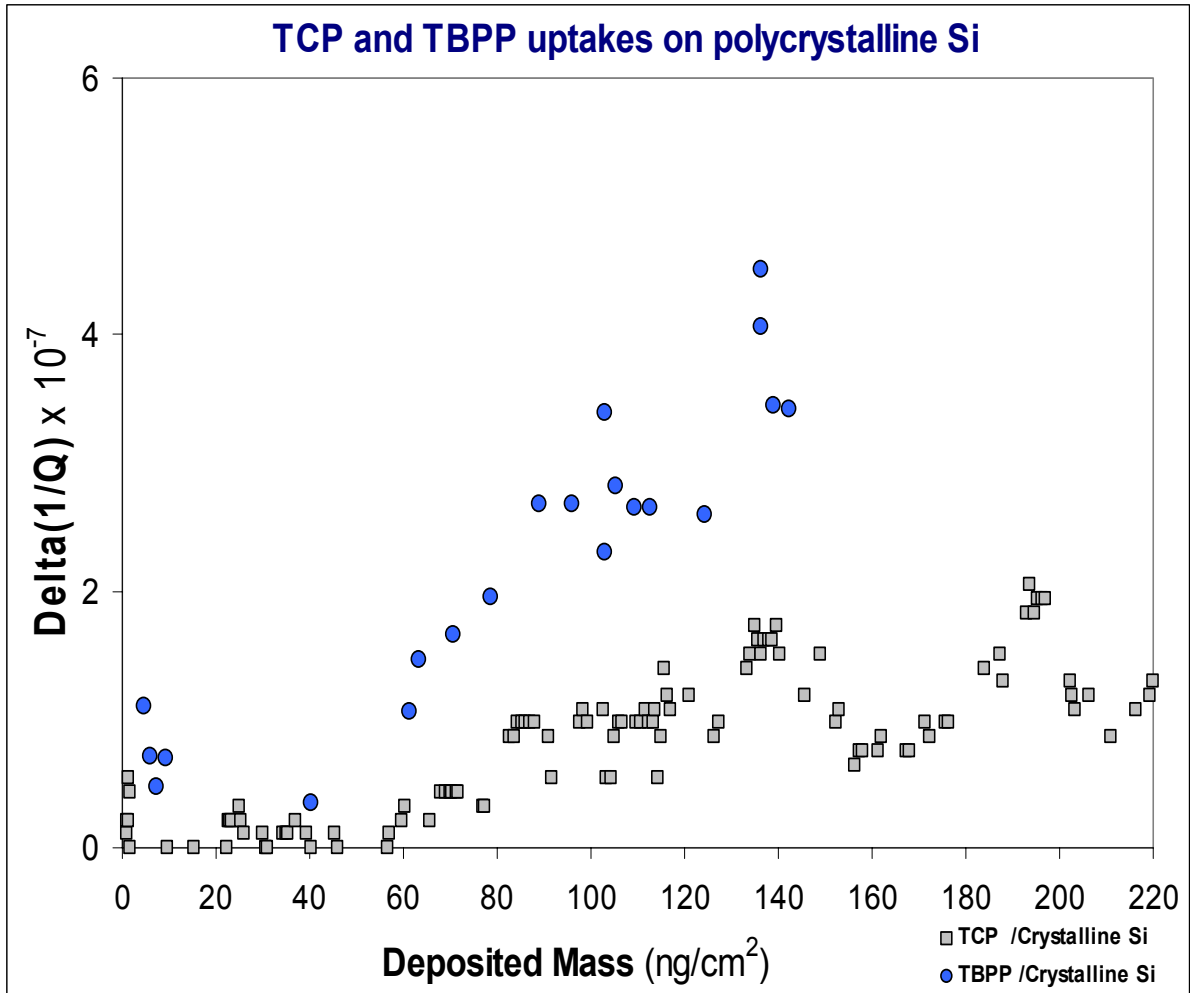


Figure 6.4 Deposited mass and Q^{-1} shift data for TCP uptake on polycrystalline silicon oxide surface (filled squares) and TBPP uptake on polycrystalline silicon oxide surface (filled circles).

6.2.3 TCP and TBPP uptakes on OTS-coated silicon surface

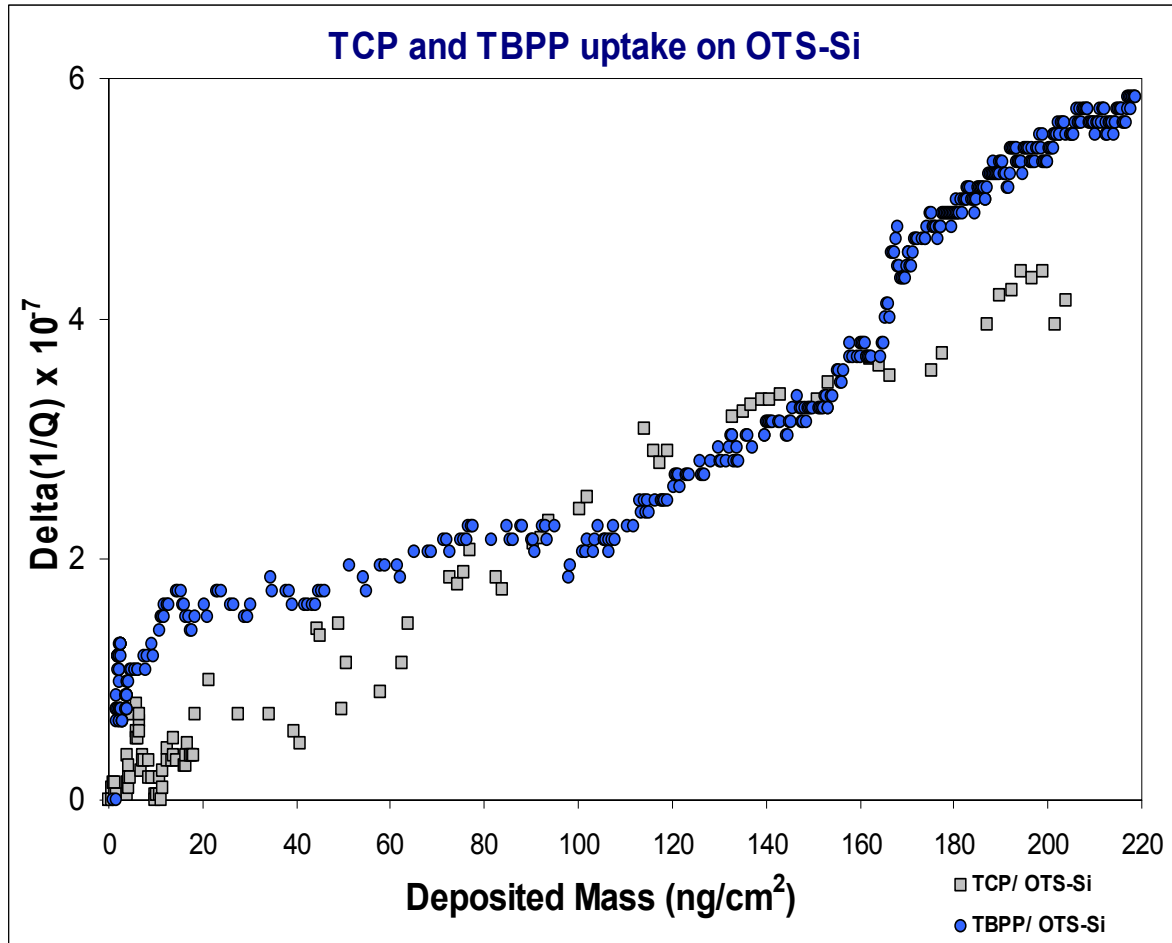


Figure 6.5 Deposited mass and Q^{-1} shift data for TCP uptake on OTS-coated silicon surface (filled squares) and TBPP uptake on OTS-coated silicon surface (filled circles).

Adsorption of TCP and TBPP on OTS-coated silicon

Figure 6.5 presents deposited mass and inverse quality factor shift data for vapor phase lubricant (TBPP and TCP) adsorption on ozone-cleaned and OTS-coated polycrystalline silicon at room temperature. Both TCP and TBPP uptakes are very similar with slightly smaller slippage in the case of TBPP.

The inverse quality factor data reveal that TCP readily slides on the OTS-coated silicon surface, characterized by slip times on the order of 0.48 ns. The slip time for TBPP is slightly shorter (0.24ns). The results are summarized in the third column of Table 1.

6.3 Surface Analysis

The below figure shows the Auger surface scan of the vapor phase lubricant exposed/OTS-coated silicon surfaces after 1 hour run. The main species that dominate the surface are carbon and oxygen. For TCP case, phosphorus is obviously seen. However, there is not much phosphorus in the TCP case (see Fig 6.6 bottom). This could be because of there was not much uptake of TCP on that particular sample. Since TCP coverage was not quite 100%, Chlorine from the OTS layer is obviously shows up on the scan. If OTS coverage is 100%, there will be no Cl left on the surface. However, this is not the case since coving the surface with one monolayer of OTS is proven to be very difficult [35]. This could explain why Cl peak shows up in Auger scan.

To confirm the morphology of silicon surface, the AFM scans were obtained with an Autoprobe M5 AFM in contact mode. In Figure 6.7, AFM images show surface morphology of amorphous silicon surface from Maxtek and polycrystalline silicon surface. The scans clearly indicate a corrugated surface, with an rms roughness that varied between 8-20 nm, and average roughness that varies between 6-15 nm. Figure A2 and A3 of Appendix A, show polycrystalline silicon surface that were grown at different temperature. The growth temperature range is from 350 C to 400 °C, only the crystals grown at 400 °C were used in this study. As shown in Fig A2 and A3, the surface roughness increases with higher growth temperature.

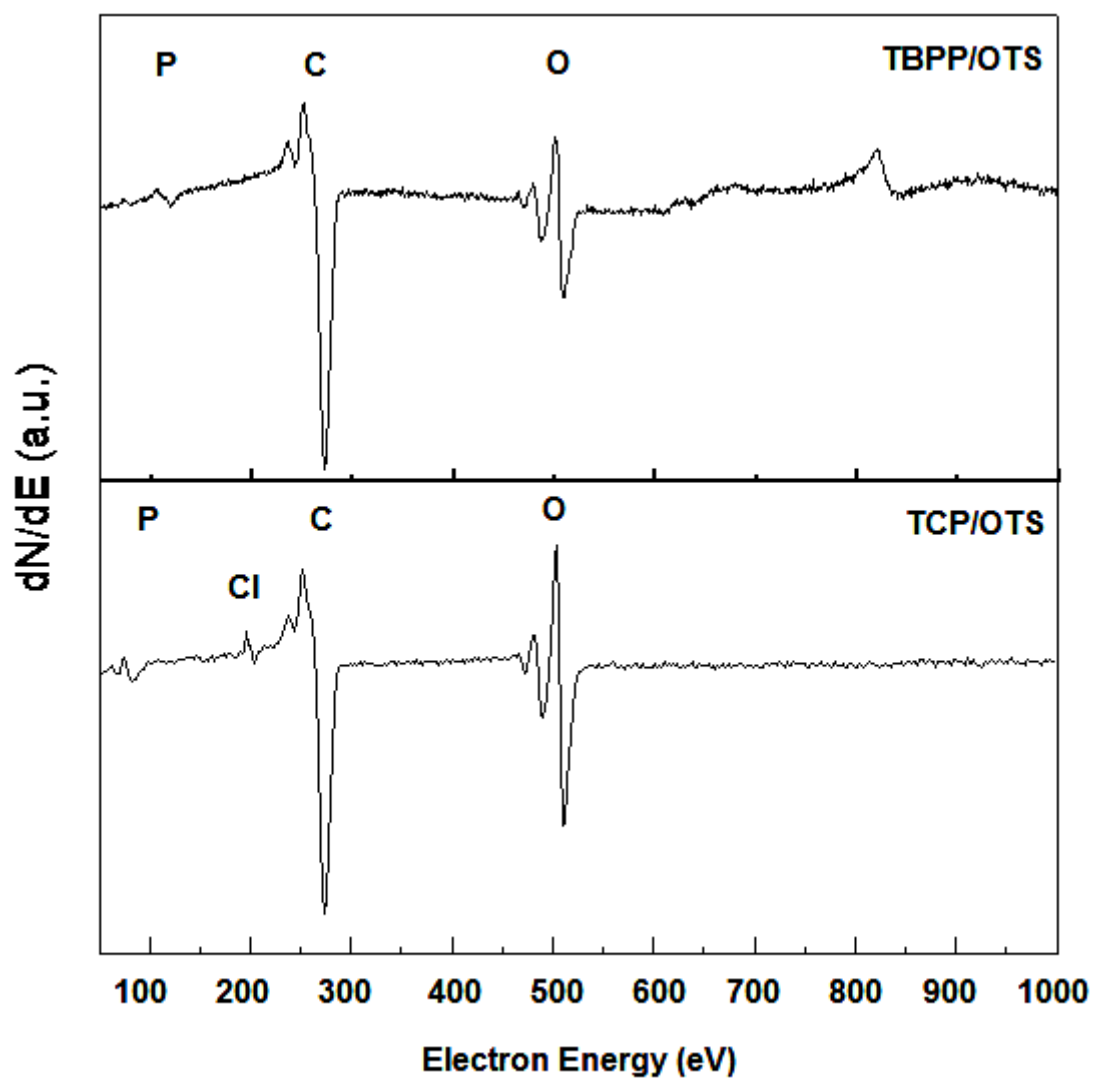


Figure 6.6 Auger Surface scans of VPL/OTS-coated silicon surface.

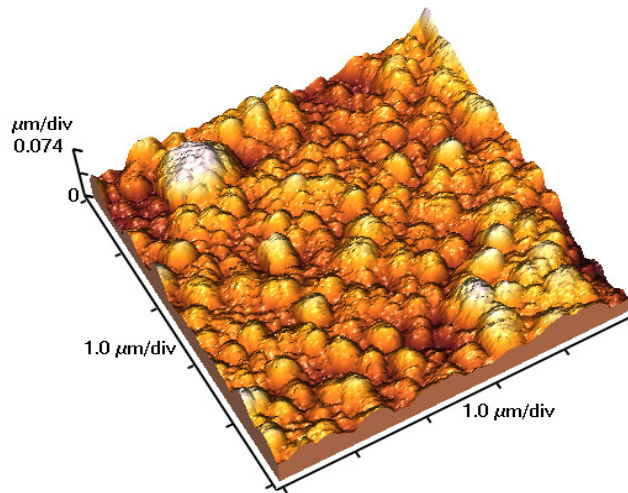
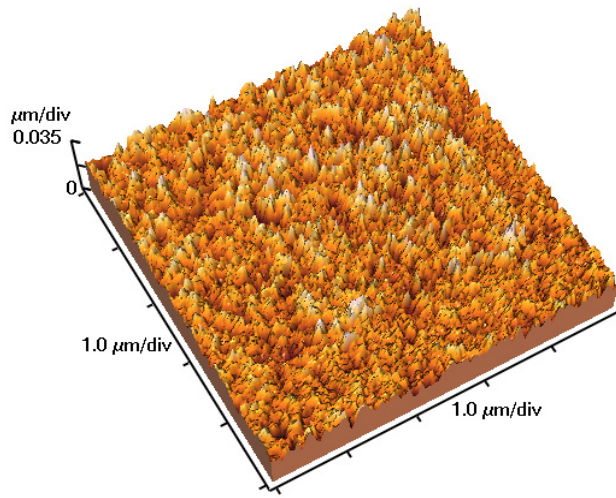


Figure 6.7 AFM images showing the surface morphology of an amorphous commercial silicon QCM crystal from Maxtek Inc. (RMS=6.31nm) (top) and a polycrystalline silicon crystal on top of SiGe/Ti/Cu QCM crystal (RMS=18.42nm) (bottom).
[Data file: Si_QCM_AFM_MURI_100705.ppt]

6.4 Discussion

From the results, we conclude that the organo-phosphate and organophosphate+OTS combinations that are slipping are all potential candidates for silicon MEMS systems. There is a strong possibility that this combination will also exhibit synergistic tribological behaviors when tested on actual MEMS devices. All silicon samples in this study were exposed to air during preparation though we tried to minimize it. Therefore, it's important to note that thin oxide layer and some hydrocarbon could exist on our silicon samples. Table 6.1 shows the summary of experimental results from vapor phase lubricant uptake.

Table 6.1 Summary of experimental results from TBPP and TCP uptake on polycrystalline silicon, amorphous silicon and OTS-coated silicon surfaces. The film thickness is listed in units of monolayer.

Vapor Phase Lubricant	Polycrystalline Silicon oxide		Ozone-cleaned amorphouse silicon oxide surface		Si oxide +OTS	
	Film thickness (monolayer)	Slip time τ (ns)	Film thickness (monolayer)	Slip time τ (ns)	Film thickness (monolayer)	Slip time τ (ns)
TCP	5	0.14	5	0.90	5	0.48
TBPP	3	0.25	5	0.30	5	0.24

However, here, we will make an attempt in explaining some interesting points from the data. First of all, the slip time of the combination of mobile lubricant (OTS) and vapor phase lubricant (TCP and TBPP) is shorter. It is suggested the lubricant film slips better without the OTS. Do we still need OTS for MEMS lubrication purposes? The answer is yes since we never know if the actual MEMS devices may perform better with a little bit of

slippery vapor phase lubricant and mobile lubricant (OTS). The combination is definitely worth studying with the actual MEMS devices. Figure 6.6 shows the Auger surface scan of the vapor phase lubricant exposed/OTS-coated silicon surfaces after 1 hour run. We observed the Chlorine peak in the scan, which shows that the OTS coverage is not quite 100%. It is known that it is difficult to obtain a uniform coating of OTS on surface. Why is this important to our experimental data?

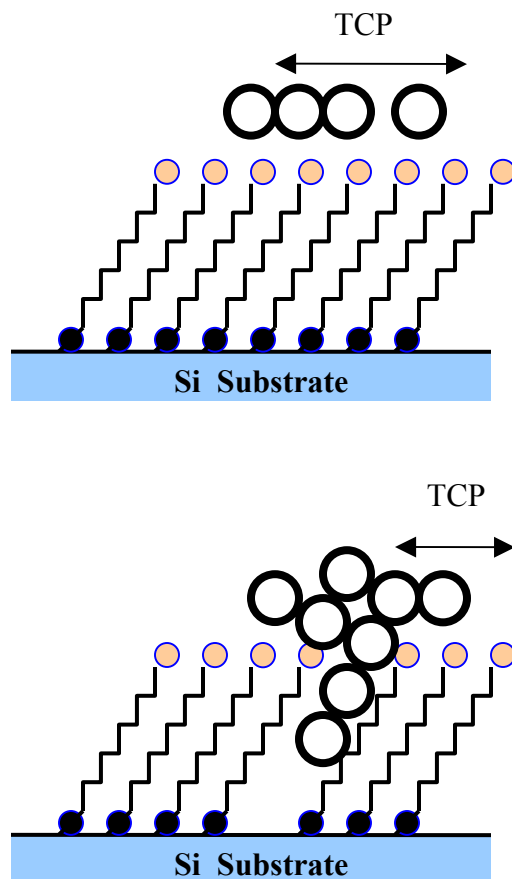


Figure 6.8 Illustration showing how the TCP molecules could get trapped in the void and slow down the mobility of the TCP film. TCP is represent with the big open circle. The structure of SAMs consists of chemisorbing headgroup (black circles : Si), backbone (hydrocarbod chain) and tail (lightly shaded circles : CH₃)[33]

If we have a close-packed OTS layer on top of quartz crystal surface, the top of the layer will be all CH₃ groups. TCP molecules would only see CH₃ groups as shown in Fig. 6.8. From molecular dynamic simulation of TCP and OTS layer, it shows the attractive force between TCP molecules is significantly larger than the attractive force between TCP and CH₃ group [55]. Therefore, TCP molecules remain mobile on the surface terminated by an OTS layer. When there are voids in the layer, or the coating is not uniform, the TCP molecules are likely to fall into the gap and become immobilized along the side walls of the OTS chain (or hydrocarbon chain)[55]. As a result, the other TCP molecules are likely to stay close to the trapped molecules because of high attractive force between each other. Figure 6.8 illustrates the effect for only couple of TCP molecules and OTS molecules. However, as a whole, this definitely slows down the oscillation of TCP film on top of non-uniform OTS layer. We also observed the same effect happening when TBPP, which is in the same lubricating family with TCP, is used. Further molecular dynamic simulation study should be able to support this conclusion. The length of the hydrocarbon chain could have an impact on TCP molecules, which can be studied more in depth using SAM with different length of hydrocarbon chain.

The combination system with bound and mobile lubricant may have slightly shorter slip time. The results of this study provide several significant insights into the potential use of TCP molecules on an OTS SAM as an effective bound+mobile lubricating system. The TCP molecules appear sufficiently mobile on a close-packed SAM surface and demonstrate the ability to transport themselves to the defected or damaged sites. This is important to OTS layer since OTS is extremely sensitive to the operation environment and deteriorates at a relatively low temperature. Furthermore, because it is deposited in solution, there is no mean

for *in situ* replenishing of lubricant coating. With TCP coating on top of OTS, this can add the ability for *in situ* replenishment in order to reduce friction and wear.

CHAPTER 7

MEMS APPLICATION

7.1 MEMS Structure

Microelectromechanical systems are the integration of miniaturized mechanical components with microelectronic components. Friction testers from Sandia National Labs are specially designed tribology test structures used to determine the friction between micromachine structural elements. The devices are designed to produce sliding contact between two etched surfaces. From the results in the previous chapters, there is a strong possibility that the combination of organophosphates and SAMS will exhibit synergistic tribological behaviors when tested on these actual MEMS devices. In this chapter, we will discuss how these friction testers work how they can be used for friction measurements in the vacuum system.

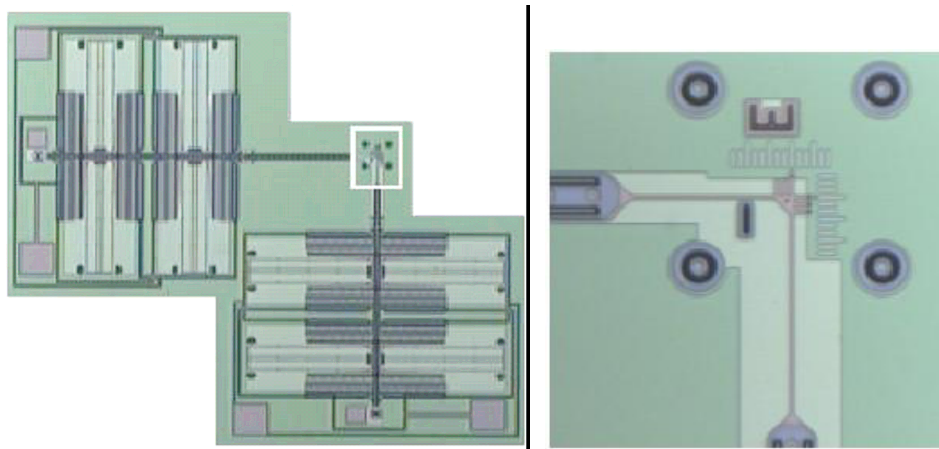


Figure 7.1 Overall view of the sidewall friction tester (left) and a close-up image of the boxed area (right) (Courtesy of M. Dugger, Sandia National Laboratory) [32].

The friction testers, which are surface micromachined sidewall tribometers, were specially designed by Sandia National Laboratories to determine the friction coefficients of the micromachined structures. Five dies, each having four friction testers were obtained. The devices were not released when they were received from Sandia national lab. These sidewall tribometers were fabricated using SUMMiT technology process. They were then sent for release at MCNC. The released samples were released using supercritical CO₂ technique, in order to avoid stiction during releasing.

Each die was then wire-bonded in a 64-pin DIP package. One of the samples was wire-bonded using a Gold ball bonder. The remaining dies were wire-bonded using Aluminum manual wedge bonder. The Figure 7.2 illustrates the wire bonding in a 64-pin package.

7.2 Friction Coefficient

Friction testers from Sandia National Labs are specially designed tribology test structures used to determine the friction between micromachine structural elements. The devices are designed to produce sliding contact between two etched surfaces (sidewalls that are perpendicular to the wafer. A schematic of the test structure is shown in the following figure.

Figure 7.2 shows a closer look of the circled area in the above wire-bonding diagram. The device is driven using two electrostatic comb-drives. One is used to pull a suspended beam into contact with a fixed semi-cylindrical post, and the other is used to oscillate the beam against the post under a load. The following figure briefly illustrates the orientation of the two comb-drives with respect to each other.

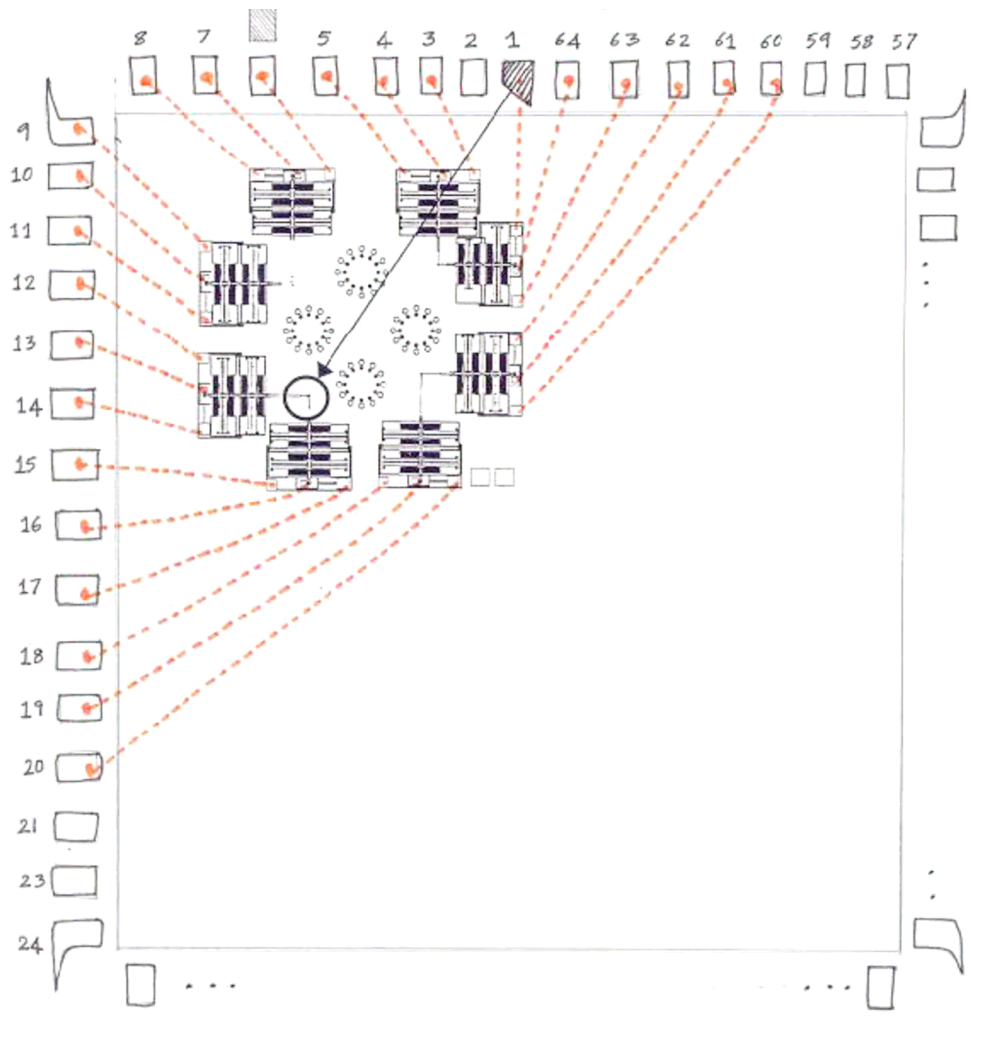


Figure 7.2 Wire-bonding diagram of the first generation of friction tester.

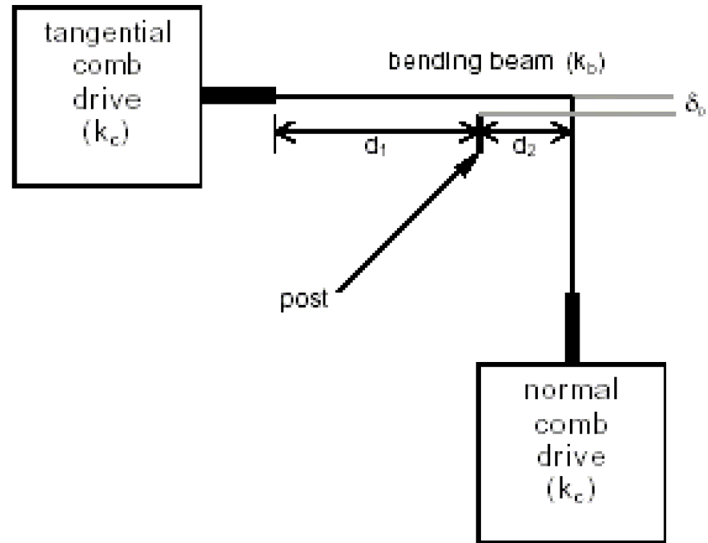


Figure 7.3 A diagram of the area where contact is made.

The polycrystalline silicon post is about $6\mu\text{m}$ high, which is deposited close to the suspended beam by low-pressure chemical vapor deposition of silicon in a deeply etched trench. The radius of curvature of the post is $2\mu\text{m}$. Figure 7.4 gives a closer view of the beam and the post where the contact is made.

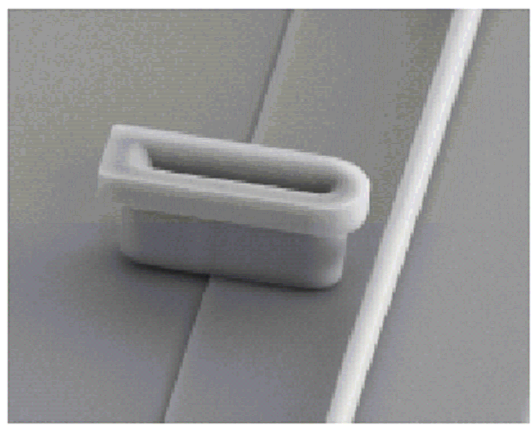


Figure 7.4 Closer view of the area where contact is made [56].

The normal comb drive (N drive), which acts perpendicular to the axis of the flexible polycrystalline silicon beam, loads the beam in contact with the post. This normal load is determined from the deflection of the comb as a function of voltage, the electrostatic force constant, and the spring constants of the comb suspension. The beam is then oscillated with respect to the fixed post using the tangential comb-drive (T drive), which acts parallel to the axis of the beam.

The friction force between the post and the beam is determined from the difference in displacement, when the test device is in contact and out of contact with the fixed post. The electrostatic force produced by the comb-drive is given by,

$$F_C = \frac{1}{2} \frac{(N t \epsilon_0 \epsilon_r V^2)}{g} \quad (7.1)$$

where V is the applied electric potential, N is the number of fingers, ϵ_0 is the permittivity in free space, ϵ_r is the relative permittivity of the dielectric material between the two electrodes (fingers), t is the thickness of the finger, and g is the gap between the two fingers.

Under equilibrium conditions, the electrostatic force is equal to the restoration force associated with the stiffness of the comb-drive system due to its displacement, giving

$$F_C = \frac{(N t \epsilon_0 \epsilon_r V^2)}{2g} = (k_c + k_b) \cdot \delta_0 \quad (7.2)$$

where k_c is the stiffness of the comb suspension springs, k_b is the stiffness of the beam in bending and δ_0 is the displacement of the comb-drive. When the comb-drive is in motion, in the absence of contact, the force balance yields,

$$F_C - (k_c + k_b) x_0 = m \frac{d^2 x_0}{dt^2} \quad (7.3)$$

where x_0 is the displacement of the comb-drive at any point in time in the absence of the load. When the suspended beam is pulled in contact with the post, a frictional drag force fd is created, and the force balance becomes,

$$F_C - (k_c + k_b) x - fd = m \frac{d^2 x_0}{dt^2} \quad (7.4)$$

where x is the displacement of the comb-drive at any point in time in the presence of contact.

As the system reaches equilibrium,

$$\frac{d^2 x_0}{dt^2} \rightarrow 0$$

$$x_0 \rightarrow \delta_0 \quad \text{and} \quad x \rightarrow \delta$$

where δ and δ_0 are the equilibrium displacements with and without friction respectively.

Since the electrostatic force in the comb drive is the same in both the cases, equations (3) and (4) may be expressed in terms of F_C , equated and solved for f_d , yielding,

$$f_d = (k_c + k_b) (\delta_0 - \delta) \quad (7.5)$$

Substituting for $(k_c + k_b)$ from equation (2),

$$f_d = (F_C / \delta_0) \cdot (\delta_0 - \delta) \quad (7.6)$$

$$f_d = F_C (1 - \delta / \delta_0) \quad (7.7)$$

The friction co-efficient is then obtained by dividing the frictional force by the applied normal load (electrostatic force associated with the normal comb-drive). Each friction test structure, which includes the tangential comb-drive and the normal-comb drive, requires five signal lines to operate. Two of the drive signals are the oscillating voltages, 180° out of phase, with $V_{p-p} \approx 50V - 60V$, and oscillating frequency of 100Hz. These signals

are used to drive the tangential comb-drive, which oscillates the beam against the fixed post driven by a square wave output (100Hz).

The other two drive signals are push/pull DC voltages with amplitude $\pm 40\text{V}$. These drive signals are used to pull the suspended beam in contact with the post. The fifth signal line is the reference/ ground line.

The friction co-efficient is then obtained by dividing the frictional force by the applied normal load (electrostatic force associated with the normal comb-drive). Each friction test structure, which includes the tangential comb-drive and the normal-comb drive, requires five signal lines to operate. Two of the drive signals are the oscillating voltages, 180° out of phase, with $V_{p-p} \approx 50\text{V} - 60\text{V}$, and oscillating frequency of 100 Hz. These signals are used to drive the tangential comb-drive, which oscillates the beam against the fixed post driven by a square wave output (100 Hz).

The other two drive signals are push/pull DC voltages with amplitude $\pm 40\text{V}$. These drive signals are used to pull the suspended beam in contact with the post. The fifth signal line is the reference/ ground line.

In this study, we quantify the amplitude of the beam position at the beam/post interface using a novel optical technique. A laser beam is made to focus on the test structure, the reflected beam is then sensed by a photo-detector circuit, which converts the light intensity into a corresponding voltage. The amount of light falling on the photo-diode depends on the amplitude of motion of the friction-tester. Several samples of the output voltages, with the beam not in contact are acquired to determine the amplitude of the beam motion without friction at the beam/post interface. A DC voltage is then applied to bring the beam in contact with the post. The output voltages are recorded as the device is run for

several cycles after loading. Once the displacement of the beam is obtained, the friction coefficient is calculated as shown above.

7.3 The Comb drive Theory

Comb drives consist of a set of fixed electrodes (or fingers) and a set of movable electrodes (or fingers) placed interdigitated with each other (see figure 7.5). The driving principle of the electrostatic Comb-Drive actuator is based on electrostatics [57].

Figure 7.5 shows a Comb-Drive actuator. When voltage is applied to the movable electrodes while the fixed electrodes are potentially grounded, a potential difference develops across the fingers and they become electrically charged. This action induces a capacitance in the charged electrodes. This results in an electrostatic force being generated, causing a displacement in the x direction. The force F created in the comb is given by,

$$F_C = \frac{1}{2} \frac{(N t \epsilon_0 \epsilon_r V^2)}{g}$$

where V is the applied electric potential, ϵ_r is the relative permittivity of the dielectric material between the two electrodes, ϵ_0 is the permittivity in the free space equal to 8.85 pF/m, n is the number of pairs of electrodes (fingers), t is the thickness of the finger, and g is the gap between the two fingers.

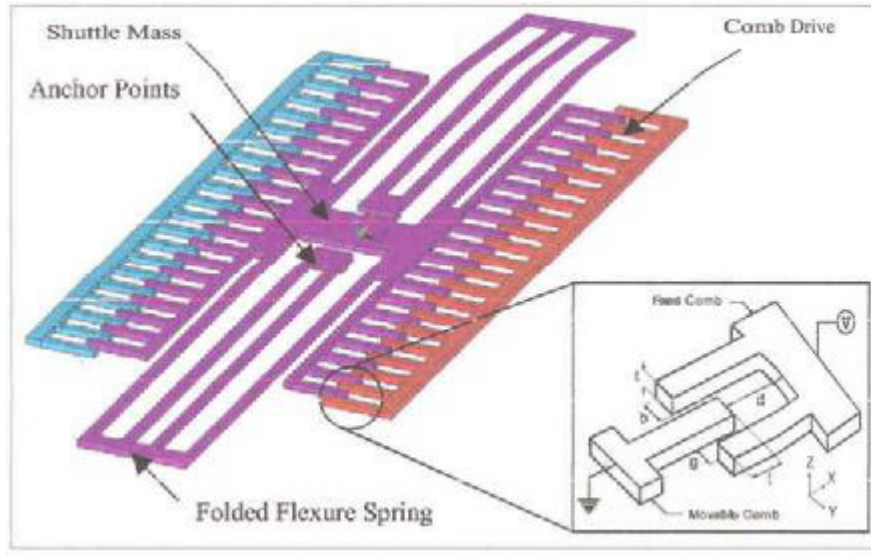


Figure 7.5 The schematic diagram of the MEMS comb drive [57].

A reaction force F_S is induced in the suspension beam holding the movable set of fingers. This suspension beam, which represents a spring suspension system, is related to the stiffness of the beam and the displacement. The relationship is given by the following equation:

$$F_S = K_X \cdot X \quad (7.)$$

In the equation K_X is the spring stiffness in the direction of actuation, and x is the displacement. If the beam stiffness is higher, a larger electrostatic force is required to cause the deflection, which means a higher driving voltage is required. In the equilibrium position, the forces F and F_S are equal.

7.4 Experimental Setup

After wirebonding the MEMS devices onto the 64-pin ceramic chip, the ceramic chip was placed in the custom-made ceramic holder which is vacuum compatible. The holder was

then placed a in a vacuum chamber and the whole experimental set-up was mounted on a vibration isolation system as shown in below figure. The vacuum chamber is connected to an ion pump and a turbo pump.

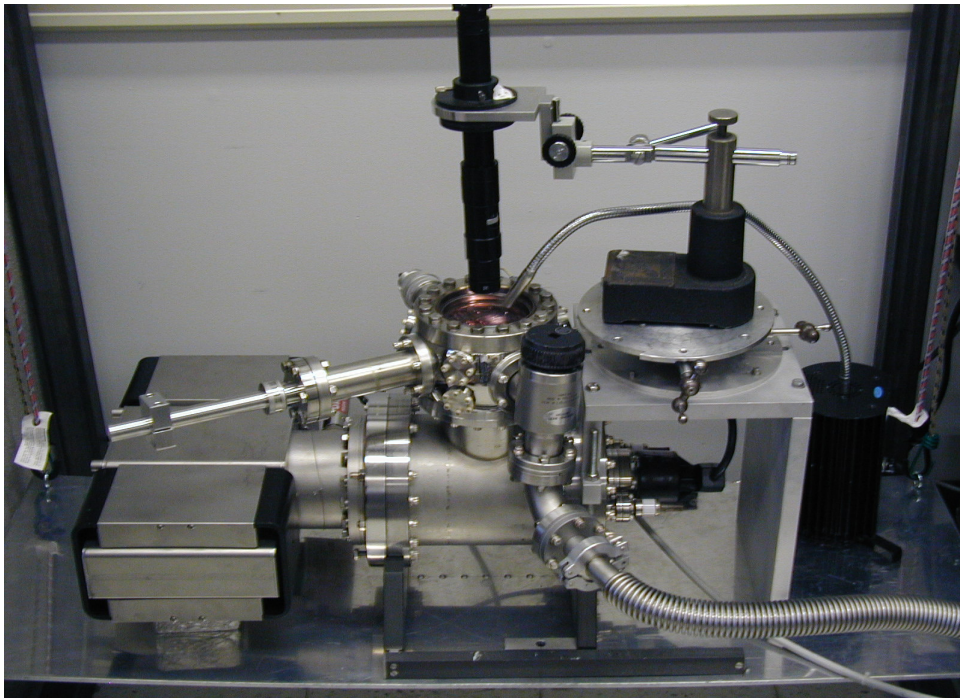


Figure 7.6 The vacuum system housing the MEMS devices

Figure 7.7 shows a closer look of how the device is mounted on the sample holder. The MEMS devices are controlled by external driving circuit via electrical feed through connection. The main chamber also connected to the laser detection system. A laser beam is made to focus on the test structure. The reflected beam is then sensed by a photo-detector circuit, which converts the light intensity into a corresponding voltage. The amount of light falling on the photo-diode depends on the amplitude of motion of the friction-tester. This laser detector is designed to detect the movement of MEMS devices in real time.

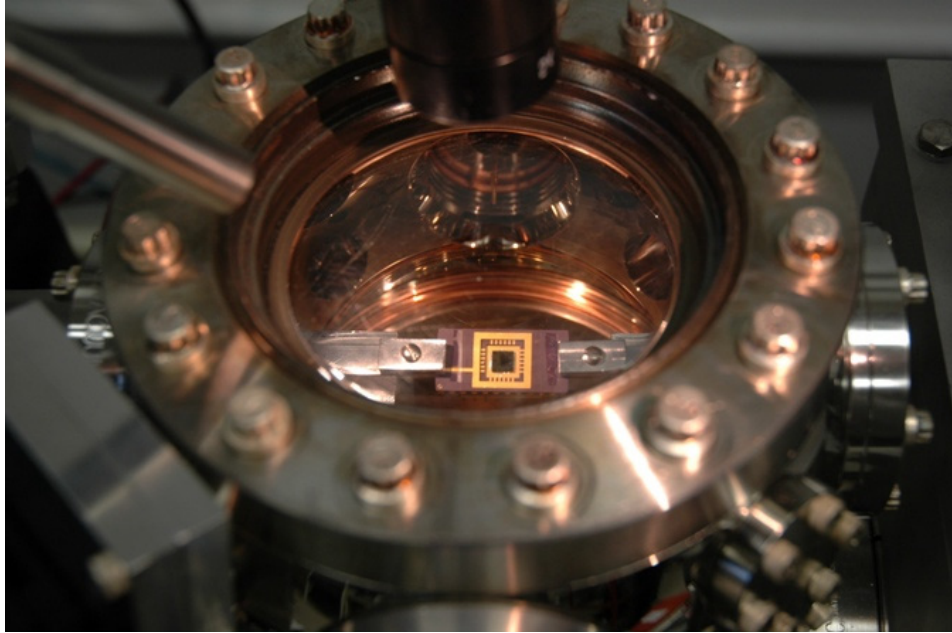


Figure 7.7 The vacuum system houses the MEMS devices wirebonded onto the ceramic chip and connected to outer equipment via electrical feedthrough.

CHAPTER 8

CONCLUSION AND FUTURE WORK

8.1 Impact of environmental gas to the water film layer

The structure and mechanical properties of fluids at solid surfaces is important in many phenomena such as lubrication, adhesion, wetting and microfluidics. For several hundred years one usually relies on the assumption that, when fluid flows over a solid surface, the liquid molecules adjacent to the solid are stationary relative to the solid and the viscosity is equal to the bulk viscosity. Though this might be a good assumption for macroscopic systems, it is questionable at molecular dimensions [1]. As discussed before, several experiments and simulations show that the textbook assumption of no slip at the boundary is not always true.

The recent progress in nanotribology clearly shows that the laws of macroscopic friction are inapplicable at the atomic scale. Though it was not carried out in the vacuum, the surface force apparatus measurements done by Granick group suggested that the slip may depend on the surrounding gases. Granick et al. discover the systematic deviations from the predictions based on the no-slip boundary condition. Their experimental results show massive deviations from this prediction were found when the tetradecane was saturated with argon. Their experimental results also showed the no-slip condition was obeyed when the tetradecane had been saturated with carbon dioxide gas [5]. However, their result does not quantitatively explain the friction coefficient difference of each system at the surface. It only reveals the important clue that the surrounding gas may influences the slippages. Our QCM

studies in vacuum strongly confirm that environmental gas definitely has an impact on the slip time of water vapor film. The water film slips very much less when there is no environmental gas. Slip times were calculated for each system with the same thickness: the slip time of water vapor film uptake in vacuum is 0.23 ns. With the present of Ar gas and N₂ gas, the calculated slip times are 4.22 and 20.37 ns, accordingly. In another word, water film moves more freely with less friction in N₂ and Ar environment. This result makes us wonder how MEMS devices work in different environment. Will their operation lifetime increases with the right surrounding? Together with the right surface coating, can this be the beginning of commercializing MEMS devices with in-contact moving parts. The result could have dramatic impact to the MEMS industry.

8.2 Future work

Future work that can be done based on this study. Since the result suggests the type of surrounding gas is very important. It will be interesting to perform the QCM experiment with different type of gas or different type of the surface at various temperature points.

The good candidates for other gas types are any gases that surround the MEMS device and may have an impact on their operation lifetime: for example, oxygen, nitrogen, argon and alcohols. Nitrogen and argon were already studied here. If oxygen were used in this experiment, the plot of the change in inverse quality factor of oxygen should be similar to Figure 5.3. The oxygen result should line in between the nitrogen data line and argon data line since the solubility coefficient of oxygen is in between nitrogen and argon solubility coefficients. Also, it can be because of the hydrophobicity of water with oxygen surrounding will fall in between nitrogen and argon number (see Table 5.3).

Table 8.1 The solubility of gas in water

Type of Gas	Solubility in water (Vol/Vol)
N ₂	0.0234
O ₂	0.0489
Ar	0.0537

Another interesting gas is alcohols (such as ethanol, propanol, butanol and pentanol) and alcohols can be hydrophilic and hydrophobic easily combining with water on one end and combining with other compounds on the other. If alcohol were to be studied, it is expected to see small change in inverse quality factor. This is because alcohol is able to combine with water easily. However, it also depends on how the other end reacts to the solid surface. Recent study by Strawhecker et al. at Pennsylvania State University indicates that alcohols molecules helps reducing the friction on MEMS the surface [50]. They reported that adhesion force drops by 40%, compared to the dry Ar case. The researchers tested the gas lubricants at various vapor pressures and find that they produce a thin film across a wide range. The small size of the alcohol molecules allows them to coat fine details of the tiny machines and the presence of gas around the MEMS makes the system self-repairing. As the thin layer wears away, more lubricant condenses to heal the area. The thin films do not interfere with either mechanical or electrical operation.

Therefore, this study can be further investigated by varying the type of the surface, the temperature and the amount of dissolved gas:

1. Different Surface: not only is the environmental gas in water important, but also the type of the surface. The type of surface will determine the binding energy and how well

gas molecules stick to the surface. Silicon and Nickel surfaces are good candidate. Silicon is what the MEMS is made of and Nickel is selected to be used in other friction study in our group.

2. Different Temperature : varying the temperature will change how gas molecules react to the surface since sticking coefficient is temperature dependence. Solubility coefficients differ for different gases and are also temperature dependent. According to Henry's law, the higher the temperature, the less gas will dissolve in a given volume of liquid. Therefore, we can expect to see more slippage of both systems in argon and nitrogen gas environment.

3. Different amount of environmental gas : since the type of surrounding gas has an effect to the slippage of water film, varying the amount of gas in the main chamber might reveal some important result (for example, 50 Torr or 500 Torr of gas). Argon and nitrogen are both soluble in water. Argon is twice and a half more soluble in water than nitrogen. When there are more gas molecules in the chamber, we can expect to see that it will take longer for water vapor to adsorb onto surface to form a monolayer.

8.3 Vapor Phase Lubricant Uptakes

The study has shown that vapor phase lubricant being delivered in gas phase can make its way and deposit itself onto the crystal surface. This is important since MEMS structure is very complicated and some surfaces of MEMS devices are out-of-sight line.

Sliding friction levels in adsorbed monolayers can be measured experimentally by means of the quartz crystal microbalance (QCM) technique. Here we have performed a quartz crystal microbalance (QCM) study of the nanotribological properties of organo-

phosphate (tricresylphosphate and t-butyl phenylphosphate) layers adsorbed from the vapor phase onto silicon (amorphous silicon and MEMS-like polysilicon), and octadecyltrichlorosilane (OTS) treated silicon surfaces. The latter systems have been studied in order to explore whether organophosphates and OTS in combination might prove synergistic from a tribological point of view [1].

From this study result, we conclude that the organo-phosphate and organophosphate+OTS combinations that are slipping are all potential candidates for silicon MEMS systems. There is a strong possibility that this combination will also exhibit synergistic tribological behaviors when tested on actual MEMS devices. Table 1 shows the summary of experimental results from vapor phase lubricant uptake.

Table 8.2 Summary of experimental results from TBPP and TCP uptake on polycrystalline silicon, amorphous silicon and OTS-coated silicon surfaces. The film thickness is listed in units of monolayer.

Vapor Phase Lubricant	Polycrystalline Silicon oxide		Ozone-cleaned amorphous silicon oxide surface		Si oxide +OTS	
	Film thickness (monolayer)	Slip time τ (ns)	Film thickness (monolayer)	Slip time τ (ns)	Film thickness (monolayer)	Slip time τ (ns)
TCP	5	0.14	5	0.90	5	0.48
TBPP	3	0.25	5	0.30	5	0.24

There are already some works done regarding finding a better SAMS coating for MEMS. One of them is PFTS and PFTS has shown that it has higher temperature resistance than OTS and easier to obtain a uniform monolayer [35]. Therefore, it is interesting to

performed QCM measurement of vapor phase lubricant on PFTS-coated silicon surface and compare to this study.

The combination system with bound and mobile lubricant may have slightly shorter slip time. The results of this study provide several significant insights into the potential use of TCP molecules on an OTS SAM as an effective bound+mobile lubricating system. The TCP molecules appear sufficiently mobile on a close-packed SAM surface and demonstrate the ability to transport themselves to the defected or damaged sites. This is important to OTS layer since OTS is extremely sensitive to the operation environment and deteriorates at a relatively low temperature. Furthermore, because it is deposited in solution, there is no mean for *in situ* replenishing of lubricant coating. With TCP coating on top of OTS, this can add the ability for *in situ* replenishment in order to reduce friction and wear.

8.4 Outlook for MEMS application

MEMS devices are highly susceptible to surface forces that can cause suspended members to deflect towards the substrate, collapse and/or adhere permanently to the substrate. Because of large surface-area-to-volume ratios and restoring forces, which are unable to overcome, interfacial forces such as capillary, chemical, van der Waals, and electrostatic attractions, adhesion and friction are critical to the performance of MEMS.

These properties must be minimized for successful operation of the devices. Surface modification using thin organic films is one of the strategies used for minimizing the adhesion and friction. In this study, silane-based self assembled monolayers is used.

The QCM study has also shown the slip of water vapor film is depending on the surrounding gas. Since the MEMS devices are controlled by external driving circuit via electrical feed

through connection and are in the controlled vacuum system, we will be able to study how MEMS devices work in different controlled environments: hot environment or with different gas surrounding such as N₂ or alcohols. The vacuum system also connected to the laser detection system which is designed to detect the movement of MEMS devices in real time. These works are presently underway. It will be interesting to see how this study can help reducing the friction at contact point and improve the MEMS operation lifetime. Designing coatings in MEMS/NEMS technology requires a fundamental understanding of nanoscale friction and adhesion for those monolayers.

REFERENCE

- [1] E. Bonaccorso, M. Kappl, H. Butt, *Phys. Rev. Lett.* 88 (2002)
- [2] Massey, B.S. *Mechanics of Fluids* 6th edn Section 5.6 (Chapman and Hall, London 1989)
- [3] P.A. Thompson, S. Troian A general boundary condition for liquid flow at solid surfaces. *Nature* 389, 360–362
- [4] J.-L. Barrat, L. Bocquet Large slip effect at a nonwetting fluid-solid interface. *Phys. Rev. Lett.* 82, 4671–4674 (1999).
- [5] S. Granick, Y. Zhu and H. Lee *Nature Materials*, 2, 221–227 (2003).
- [6] R. Pit, H. Hervet, and L. Leger, *Phys. Rev. Lett.* 85, 980 (2000).
- [7] V. S. J. Craig, C. Neto, and D. R. M. Williams, *Phys. Rev. Lett.* 87, 4504 (2001).
- [8] Y. Zhu and S. Granick, *Phys. Rev. Lett.* 87, 96105 (2001).
- [9] D.C. Tretheway, C.D. Meinhart, Apparent fluid slip at hydrophobic microchannel walls. *Phys. Fluids* 14, L9–L12 (2002).
- [10] E. Ruckenstein, P. Rajora On the no-slip boundary condition of hydrodynamics, *J. Colloid Interface Sci.* 96, 488–493 (1983).
- [11] O. I. Vinogradova Slippage of water over hydrophobic surfaces. *Int. J. Miner. Process* 56, 31–60 (1999).
- [12] J. W. G. Tyrrell and P. Attard, Atomic force microscope images of nanobubbles on a hydrophobic surface and corresponding force-separation data. *Langmuir* 18, 160–167 (2002).

- [13] Ishida, N., Inoue, T., Miyahara, N. & Higashitani, K. Nano bubbles on a hydrophobic surface in water observed by tapping-mode atomic force microscopy. *Langmuir* 16, 6377–6380 (2000)
- [14] U.C. Boehnke et al. Partial air wetting on solvophobic surfaces in polar liquids. *J. Colloid Interface Sci.* 211, 243–251 (1999).
- [15] J. Krim Friction at the nano-scale *Physics World* 25-26 (2005).
- [16] A.R. Krauss, O. Auciello, D.M. Gruen, A. Jayatissa, A. Sumant, J. Tucek, D.C. Mancini, N. Moldovan, A. Erdemir, D. Ersoy, M.N. Gardo, H.G. Busmann, E.M. Meyer and M.Q. Ding, *Diamond and Related Materials* 10, 1952 (2001).
- [17] S. Sundararajan and B. Bhushan, *Wear* 225, 678 (1999).
- [18] D.F. Wang and K. Kato, *Tribol. Int.* 34, 407 (2001).
- [19] T.M. Mayer, J.W. Elam, S.M. George, P.G. Kotula and R.S. Goeke, *Appl. Phys. Lett.* 82, (2003) 2883.
- [20] W.R. Ashurst, C. Yau, C. Carraro, C. Lee, G.J. Kluth, R.T. Howe and R. Maboudian, *Sensors Actuators A* 91 (2001) 239.
- [21] S.T. Patton, W.D. Cowan, K.C. Eapen and J.S. Zabinski, *Tribol. Lett.* 9, 199 (2000).
- [22] S. Sundararajan and B. Bhushan, *Wear* 225, 678 (1999).
- [23] K.C. Eapen, S.T. Patton and J.S. Zabinski, *Tribol. Lett.* 12 (2002).
- [24] H. Heshmat, *Tribology Trans.* 34, 433 (1991).
- [25] C. F Higgs, C. A. Heshmat, and H. Heshmat, *ASME*, 98-Trib-1-61, 25 (1998).
- [26] M. Abdelmaksoud, J. W. Bender, and J. Krim, *Phys. Review Lett.* 92, 176101 (2004).
- [27] D.R. Wheeler, O.D. Faut, *Appl. of Surface Sci.*, 18, 106 (1984).
- [28] M. Abdelmaksoud dissertation (2001).

- [29] J. Krim and A. Widom Phys. Rev. B 38, 12184, 1988; A. Widom and J. Krim, Phys. Rev. B 34, R3, (1986)
- [30] G. Z. Sauerbrey, Phys. Verhandl., 8, 113, (1957).
- [31] G. Z. Sauerbrey, Z. Phys., 115, 206, (1959).
- [32] A. Ulman An Introduction to Ultrathin Organic Films: From Langmuir-Blodgett to Self-Assembly. Academic Press, San Diego, (1991).
- [33] F. Schreiber Structure and growth of self-assembling monolayers. Progress in Surface Sci, 65 (5-6): 151-256, (2000).
- [34] U.Srinivasan, M. R. Houston, R.T. Howe, R. Maboudian Journal of Microelectromechanical Systems 7 252-26 (1998).
- [35] W. R. Ashurst, C. Yau, C. Carraro, R. Maboudian, and M. Dugger Journal of Microelectromechanical systems, 10 (2001) .
- [36] C. D. Stockbridge Vacuum Microbalance Techniques 5 (1966).
- [37] L.D. Landau and E. M. Lifshitz, Fluid Mechanics Vol. 6 of Course of Theoretical Physics, 88-90 (1959).
- [38] H. Hlemholtz and S. Piotrowski Der k. Akad. In Wien 40 (1860).
- [39] L. Bruschi and G. Mistura Phys. Rev. B 63, 235411 (2001).
- [40] J. Krim and A. Widom Phys. Rev. B 38 12184 (1988); A.Widom, J. Krim, Phys. Rev. B 34, R3 (1986).
- [41] T. Coffey Dissertation North Carolina State University (2004).
- [42] T.A. Carlson Photoelectron and Auger Spectroscopy (1975).
- [43] A. W.Czanderna ed. Methods of Surface Analysis (1975).

- [44] J. B. Brzoska, I. Ben Azouz, and F. Rondelez. Silanization of solid substrates: A step toward reproducibility. *Langmuir*, 10(11):4367–73 (1994).
- [45] D. K. Schwartz, S. Steinberg, J. Israelachvili, and J. Zasadzinski. Growth of a self-assembled monolayer by fractal aggregation. *Physical Review Letters*, 69(23):3354–3357 (1992).
- [46] Uthara Srinivasan, Michael R. Houston, Roger T. Howe, and Roya Maboudian. Alkyltrichlorosilane-based self-assembled monolayer films for stiction reduction in silicon micro-machines. *Journal of Microelectromechanical Systems*, 7(2):252–260 (1998).
- [47] K. Efimenko, B. Novick, R. G. Carbonell, J. M. DeSimone, and J. Genzer, Formation of self-assembled monolayers of semifluorinated and hydrocarbon chlorosilane pre-cursors on silica surfaces from liquid carbon dioxide. *Langmuir*, 18(16):6170–6179 (2002).
- [48] O. I. Vinogradova *Int. J. Miner. Process* 56, 31-60 (1999).
- [49] P. G. de Gennes, On fluid/wall slippage. *Langmuir* 18 3413-3414 (2002).
- [50] K. Strawhecker, D. B. Asay and S. H. Kim, Gas-Phase Lubrication of MEMS Devices: Using Alcohol Vapor Adsorption Isotherm for Lubrication of Silicon Oxides. In *Encyclopedia of Chemical Processing*; Sunggyu Lee, Ed.; Taylor & Francis, Inc.: New York, Vol. 2, pp.1143-1150 (2005).
- [51] J. D. Jackson, *Classical Electrodynamics*, 3rd ed. John Wiley and Sons (1998)
- [52] V. Gutmann, Fundamental considerations about liquid water, *Pure Appl. Chem.* 63, 1715-1724 (1991).
- [53] E. R. Caffarena and J. R. Grigera, On the hydrogen bond structure of water at different densities, *Physica A* 342, 34-39 (2004).

- [54] D. A. Doshi, E. B. Watkins, J. N. Israelachvili and J. Majewski, Reduced water density at hydrophobic surfaces: Effect of dissolved gases, *Proc. Natl. Acad. Sci. USA*, 102, 9458-9462 (2005).
- [55] D. L. Irving and D. W. Brenner, Diffusion on a self-assembled monolayer, *Journal of Physical Chemistry B* 110 31 15426 (2006).
- [56] M. T. Dugger, D. C. Senft and G. C. Nelson, Friction and durability of chemisorbed organic lubricants for MEMS, Sandia National Laboratory.
- [57] W. A. Moussa, H. Ahmed, W. Badaway, M. Moussa, Investigating the reliability of electrostatic comb-drive actuators utilized in microfluidic and space systems using finite element analysis.

APPENDIX

APPENDIX A

QCM Quartz Crystal Sample Preparation

This is to explain a little bit more about the growing the polycrystalline silicon on top of quartz crystal samples to be use in this study. The work was done by Sang Min Lee and James Burnett from department of physics. First the gold electrodes were made on both sides of quartz crystals with metal deposition technique. Then the process of growing polycrystalline was done with molecular beam deposition (MBE). However, Si could not be grown directly on top of Au/QCM because Au would segregate through the silicon layer. As a result, it is necessary to have a buffer layer in between gold and silicon. Then silicon were grown on top at low temperature ($<500^{\circ}\text{C}$). The process was quite challenging in finding the right buffer layer and growth temperature for silicon growth in order to obtain polycrystalline surface. However, after several runs, the right buffer layer and temperature were found. Polycrystalline films were grown successfully with molecular beam deposition and characterization of polycrystalline silicon films using a Si-Ge buffer layer to initiate nucleation at temperature of 400°C .

As shown in Figure A4, Raman Spectroscopy shows the sharp feature at 520 cm^{-1} representing the triply degenerate zone center mode of crystalline silicon. The presence of crystalline silicon is confirmed by the intense peak located at 520 cm^{-1} . Any disorganization in the polycrystalline silicon is recognized by the presence of relatively broad peaks around 150 and 480 cm^{-1} . These features correspond to the broadened density of vibrational states of

the Si. The ratio intensities of ~ 520 and 480 cm^{-1} peaks in the films can be employed to determine the relative fraction of amorphous silicon in a sample.

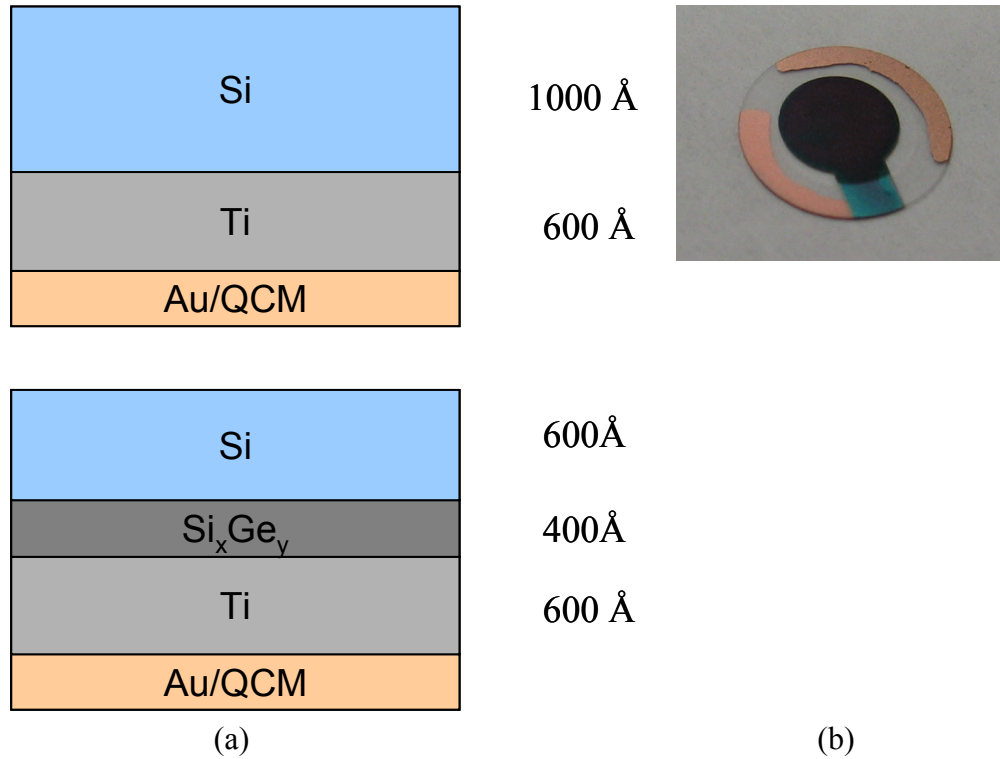


Figure A1 (a) The diagram of silicon growth with MBE on top of two possibilities of buffer layer (b) The QCM crystal sample with gold electrodes and silicon on the surface.

To confirm the morphology of silicon surface, the AFM scans were obtained with an Autoprobe M5 AFM in contact mode. The scans clearly indicate a corrugated surface, with an rms roughness that varied between 8-20 nm, and average roughness that varies between 6-15 nm. Figure A2 and A3 show polycrystalline silicon surface that were grown at different temperature. The growth temperature range is from 350 C to 400 °C, only the crystals grown at 400 C were used in this study. As shown in Fig A2 and A3, the surface roughness is increasing with increasing temperature.

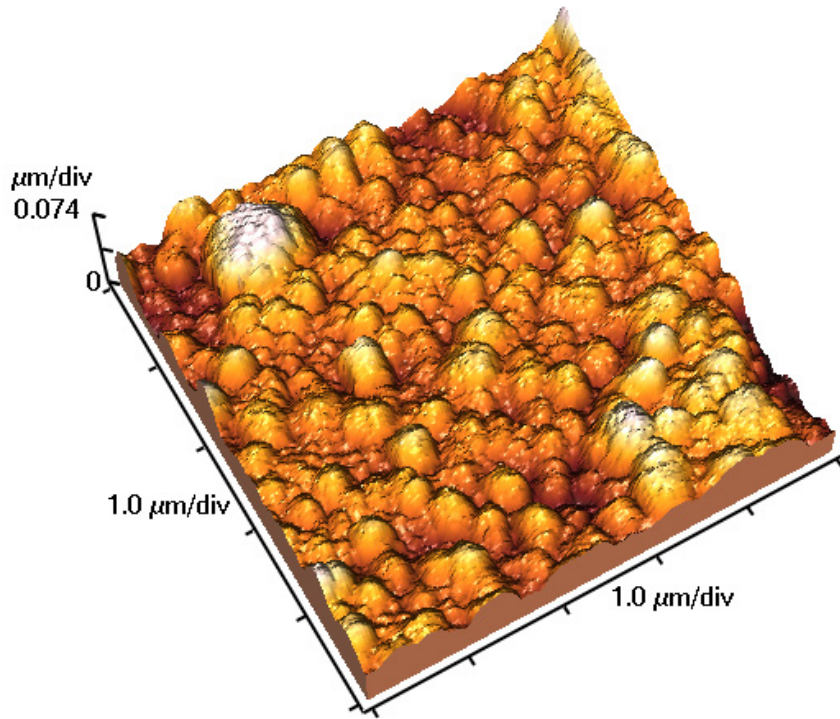


Figure A2 An AFM image of polycrystalline silicon oxide surface with growth temperature of 400 °C (RMS=18.42nm).

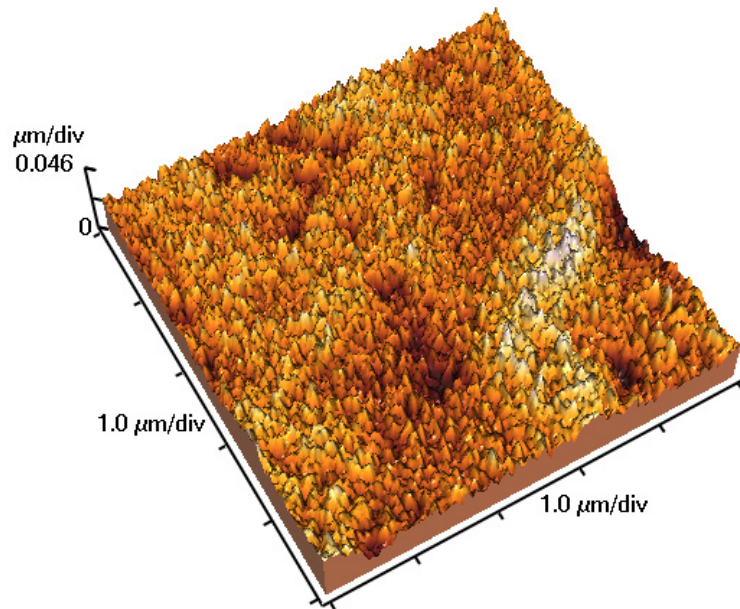
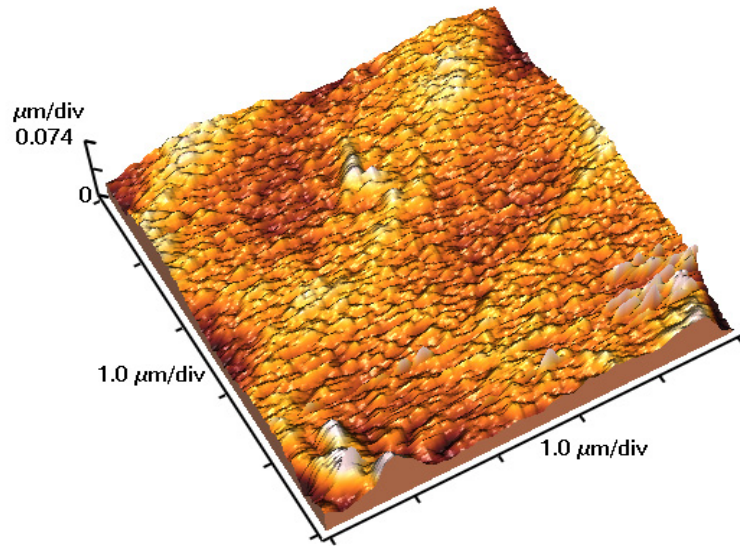


Figure A3 AFM images of polycrystalline silicon oxide surface with growth temperature of 375 °C (top: RMS = 14.43nm) and 350 °C (bottom:RMS=9.65nm)

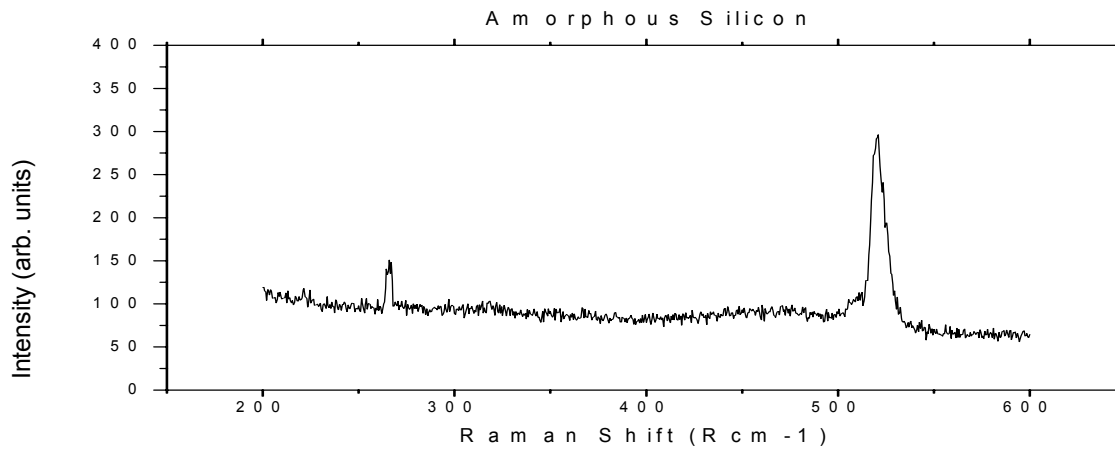
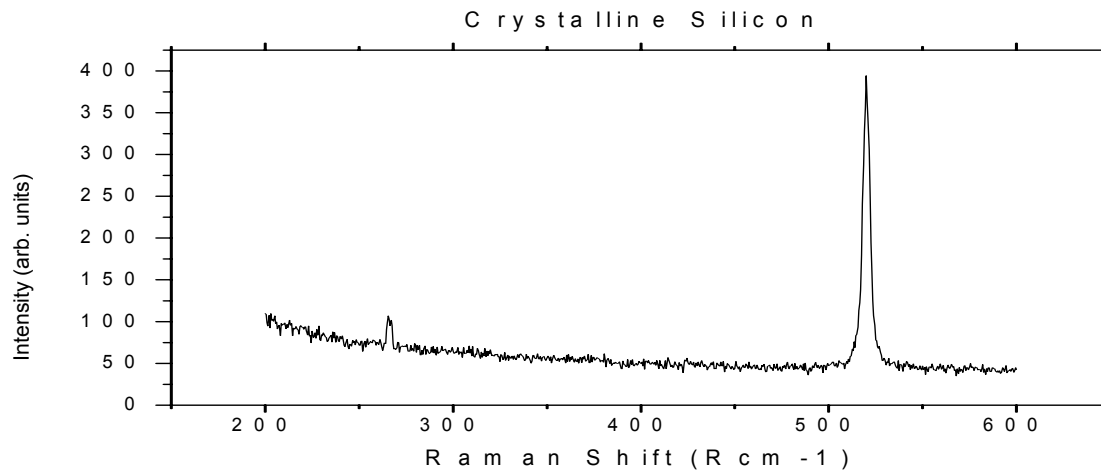


Figure A4 Raman Spectroscopy of a poly crystalline silicon film (top) and b) a film with an amorphous silicon component (bottom). The peak at $\sim 260 \text{ cm}^{-1}$ is a calibration line. data.

APPENDIX B

The Labview Program

The Labview program was rewritten based on previous program code by Mohamed Abdelmaksoud. Via GPIB connection, the Labview program can interface with multimeters for QCM uptake measurements. This allows us to measure and record the change in frequency and quality factor in real time. Figure B1 and B2 shows the front panel and block diagram.

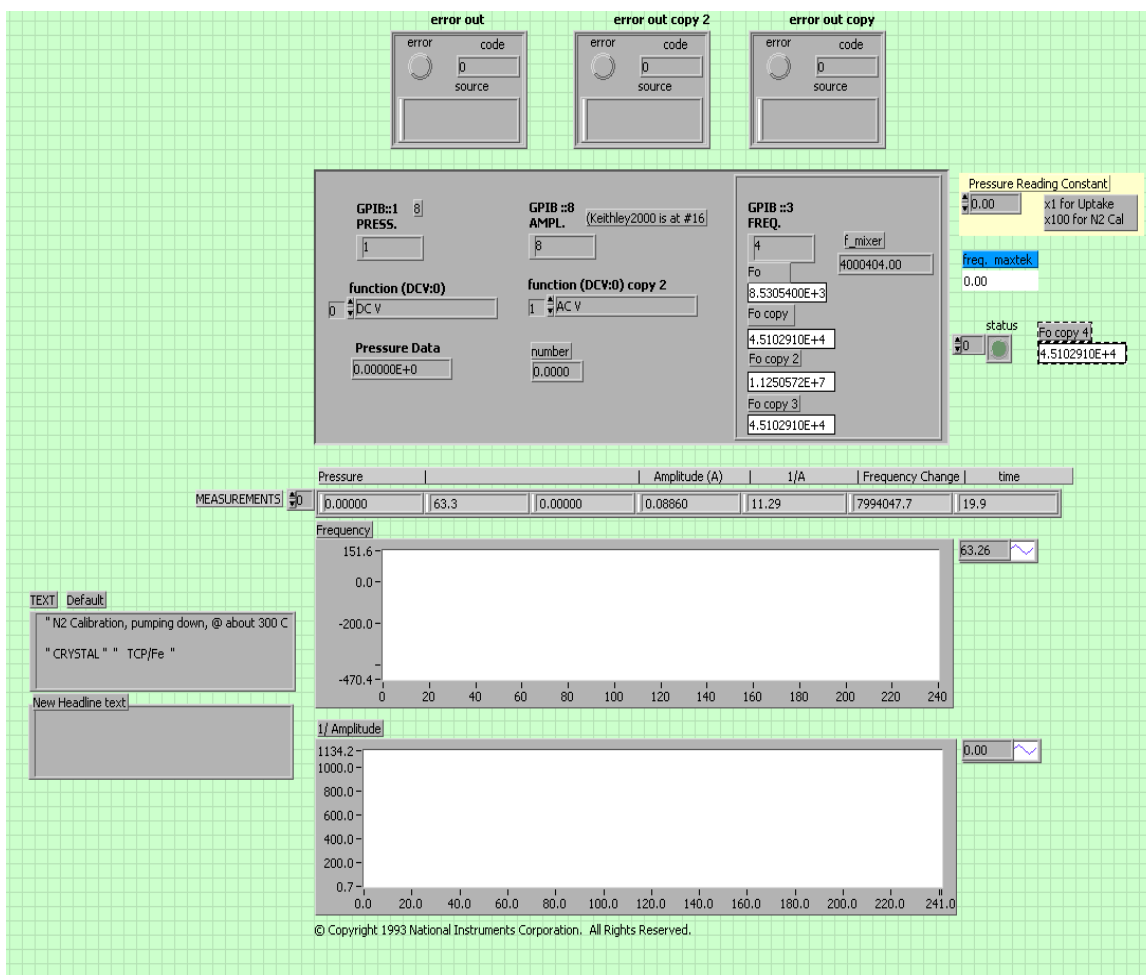


Figure B1 Show the front panel diagram of Labview program for QCM uptake measurements

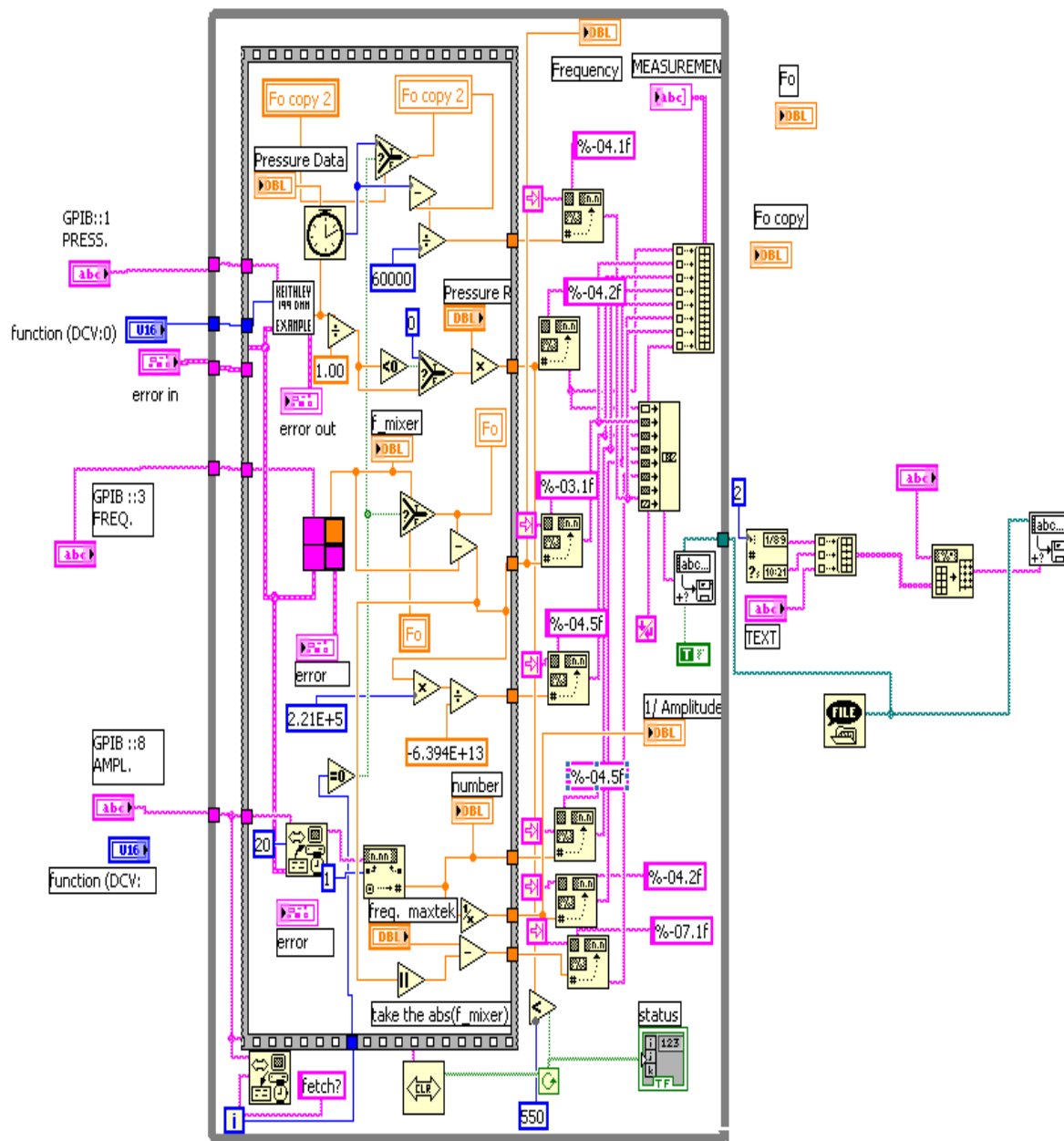


Figure B2 The block diagram of Labview program for QCM uptake measurements